

SEARCH FOR POINT SOURCES OF HIGH-ENERGY NEUTRINOS WITH AMANDA

J. AHRENS,¹ X. BAI,² G. BAROUCH,³ S. W. BARWICK,⁴ R. C. BAY,⁵ T. BECKA,¹ K.-H. BECKER,⁶ D. BERTRAND,⁷ F. BINON,⁷
A. BIRON,⁸ S. BOESER,⁸ O. BOTNER,⁹ A. BOUCHTA,^{8,10} O. BOUHALI,⁷ T. BURGESS,¹¹ S. CARIUS,¹² T. CASTERMANS,¹³
D. CHIRKIN,^{5,6} J. CONRAD,⁹ J. COOLEY,³ D. F. COWEN,¹⁴ A. DAVOUR,⁹ C. DE CLERCQ,¹⁵ T. DEYOUNG,³
P. DESIATI,³ J.-P. DEWULF,⁷ P. DOKSUS,³ J. EDSJÖ,¹¹ P. EKSTRÖM,¹¹ T. FESER,¹ T. K. GAISSER,²
M. GAUG,⁸ L. GERHARDT,⁴ A. GOLDSCHMIDT,¹⁶ A. HALLGREN,⁹ F. HALZEN,³ K. HANSON,³
R. HARDTKE,³ T. HAUSCHILDT,⁸ M. HELLWIG,¹ P. HERQUET,¹³ G. C. HILL,³ P. O. HULTH,¹¹
K. HULTQVIST,¹¹ S. HUNDERTMARK,⁴ J. JACOBSEN,¹⁶ A. KARLE,³ J. KIM,⁴ L. KÖPKE,¹
M. KOWALSKI,⁸ K. KUEHN,⁴ J. I. LAMOUREUX,¹⁶ H. LEICH,⁸ M. LEUTHOLD,⁸ P. LINDAHL,¹²
J. MADSEN,¹⁷ P. MARCINIEWSKI,⁹ H. MATIS,¹⁶ C. P. MCPARLAND,¹⁶ T. C. MILLER,^{2,18}
Y. MINAEVA,¹¹ P. MIOCINOVIĆ,⁵ P. C. MOCK,^{4,19} R. MORSE,³ T. NEUNHÖFFER,¹ P. NIESSEN,¹⁵
D. R. NYGREN,¹⁶ H. ÖGELMAN,³ P. OLBRECHTS,¹⁵ C. PÉREZ DE LOS HEROS,⁹ A. C. POHL,¹²
P. B. PRICE,⁵ G. T. PRZYBYLSKI,⁴ K. RAWLINS,³ E. RESCONI,⁸ W. RHODE,⁶ M. RIBORDY,⁸
S. RICHTER,³ J. RODRÍGUEZ MARTINO,¹¹ P. ROMENESKO,³ D. ROSS,⁴ H.-G. SANDER,¹
T. SCHMIDT,⁸ D. SCHNEIDER,³ R. SCHWARZ,³ A. SILVESTRI,⁴ M. SOLARZ,⁵ G. M. SPICZAK,¹⁷
C. SPIERING,⁸ D. STEELE,³ P. STEFFEN,⁸ R. G. STOKSTAD,¹⁶ K.-H. SULANKE,⁸ I. TABOADA,²⁰
L. THOLLANDER,¹¹ S. TILAV,² C. WALCK,¹¹ C. WEINHEIMER,¹ C. H. WIEBUSCH,^{8,10}
C. WIEDEMANN,¹¹ R. WISCHNEWSKI,⁸ H. WISSING,⁸ K. WOSCHNAGG,⁵ W. WU,⁴
G. YODH,⁴ AND S. YOUNG⁴

(THE AMANDA COLLABORATION)

Received 2002 July 26; accepted 2002 October 2

ABSTRACT

This paper describes the search for astronomical sources of high-energy neutrinos using the AMANDA-B10 detector, an array of 302 photomultiplier tubes used for the detection of Cerenkov light from upward-traveling neutrino-induced muons, buried deep in ice at the South Pole. The absolute pointing accuracy and angular resolution were studied by using coincident events between the AMANDA detector and two independent telescopes on the surface, the GASP air Cerenkov telescope and the SPASE extensive air shower array. Using data collected from 1997 April to October (130.1 days of live time), a general survey of the northern hemisphere revealed no statistically significant excess of events from any direction. The sensitivity for a flux of muon neutrinos is based on the effective detection area for through-going muons. Averaged over the northern sky, the effective detection area exceeds 10,000 m² for $E_\mu \approx 10$ TeV. Neutrinos generated in the atmosphere by cosmic-ray interactions were used to verify the predicted performance of the detector. For a source with a differential energy spectrum proportional to E_ν^{-2} and declination larger than +40°, we obtain $E^2(dN_\nu/dE) \leq 10^{-6}$ GeV cm⁻² s⁻¹ for an energy threshold of 10 GeV.

Subject headings: neutrinos — surveys

On-line material: color figures

¹ Institute of Physics, University of Mainz, Staudinger Weg 7, D-55099 Mainz, Germany.

² Bartol Research Institute, University of Delaware, Newark, DE 19716.

³ Department of Physics, University of Wisconsin, Madison, WI 53706.

⁴ Department of Physics and Astronomy, University of California, Irvine, CA 92697.

⁵ Department of Physics, University of California, Berkeley, CA 94720.

⁶ Fachbereich 8 Physik, BUGH Wuppertal, D-42097 Wuppertal, Germany.

⁷ Université Libre de Bruxelles, Science Faculty CP 230, Boulevard du Triomphe, B-1050 Brussels, Belgium.

⁸ DESY-Zeuthen, D-15735 Zeuthen, Germany.

⁹ Division of High Energy Physics, Uppsala University, S-75121 Uppsala, Sweden.

¹⁰ Current address: CERN, CH-1211 Geneva 23, Switzerland.

¹¹ Fysikum, Stockholm University, S-11385 Stockholm, Sweden.

¹² Department of Technology, University of Kalmar, S-39182 Kalmar, Sweden.

¹³ University of Mons-Hainaut, Mons, Belgium.

¹⁴ Department of Physics, Pennsylvania State University, University Park, PA 16802.

¹⁵ Vrije Universiteit Brussel, Dienst ELEM, B-1050 Brussels, Belgium.

¹⁶ Lawrence Berkeley National Laboratory, Berkeley, CA 94720.

¹⁷ Department of Physics, University of Wisconsin, River Falls, WI 54022.

¹⁸ Current address: Johns Hopkins University, Applied Physics Laboratory, Laurel, MD 20723.

¹⁹ Current address: Optical Networks Research, JDS Uniphase, 100 Willowbrook Road, Freehold, NJ 07728-2879.

²⁰ Departamento Física, University Simón Bolívar, Caracas, Venezuela.

1. INTRODUCTION

Nature provides precious few information carriers from the deep recesses of space, and it is imperative to develop techniques to exploit each one. Throughout history, the photon messenger has made vital contributions to the understanding of the observable universe. In this paper, we present results from a new generation of telescopes designed to detect a very different kind of information carrier, high-energy neutrinos (where $E_\nu > 1$ TeV). The search for astronomical sources of high-energy neutrinos is one of the central missions of the Antarctic Muon and Neutrino Detector Array (AMANDA; Wischnewski et al. 1999). In this paper, we describe a general search for continuous emission from a spatially localized direction in the northern sky,²¹ restricted to declinations greater than $+5^\circ$. The search technique is conceptually simple: a point source is identified by a statistically significant enhancement over expected background fluctuations from a particular direction. Expected background is readily obtained experimentally from off-source sky bins within the same band of declination. In contrast, unresolved, or diffuse, signals are characterized by an isotropic distribution, and backgrounds are estimated by detector simulation programs. The most favorable flux predictions for point sources are several orders of magnitude lower than the most optimistic predictions for diffusely distributed sources. However, atmospheric neutrino background is diffusely distributed as well, so the level of intrinsic background in the diffuse search is also several orders of magnitude higher. While signal-to-noise ratio considerations favor the search for diffuse emission over point-source searches, the interpretation of a diffusely distributed signal is more ambiguous. Thus, the search for point sources complements the search for diffuse sources. The latter search is described in Hill & Leuthold (2001).²² The more specific searches for point emission from gamma-ray bursters (Hardtke & Barouch 2001)²³ and quasi-pointlike emission from Galactic dark matter trapped in the core of the Earth (Ahrens et al. 2002b) are presented in separate papers since these analyses were optimized for different flux spectra and different background characteristics.

2. MOTIVATION

The origin of cosmic rays is one of the oldest puzzles in particle astrophysics. Shocks from Galactic supernovae are widely believed to accelerate cosmic rays to $\sim 10^{15}$ eV, while the sources of cosmic rays at the most extreme energies are not known. Plausible models of particle acceleration exist for many classes of Galactic and extragalactic objects, but supporting evidence for any model is largely circumstantial. The observation of high-energy neutrinos from point sources would unequivocally confirm the hadronic nature of such accelerators. Unfortunately, the predicted neutrino fluxes from Galactic and extragalactic point sources are too low to be detected with AMANDA-B10, although

uncertainties in the model parameters lead to considerable variation in the flux predictions.

Supernova remnants (SNRs) are one of the few classes of Galactic sites that have the capability to supply sufficient power to accelerate Galactic cosmic rays. The diffusive shock mechanism naturally produces a power-law spectrum of $dN/dE \propto E^{-2.1}$, which is consistent with the deduced spectral index of cosmic rays.

Recent observations of TeV gamma rays from plerions such as the Crab Nebula and SNRs provide direct evidence for particle acceleration to high energies. However, these observations do not provide compelling evidence for *hadronic* acceleration because of an unfortunate ambiguity: it is possible (and even probable) that electrons are solely responsible for the high-energy gamma-ray production. But if SNRs are the accelerators of Galactic cosmic rays, they must also accelerate hadrons. A class of models exploits this idea by suggesting that both protons and electrons are accelerated by the supernova shock. Pions, both neutral and charged, are produced in the nuclear collisions between protons and ambient material (a cosmic equivalent of a “beam dump” commonly used by terrestrial accelerators) and then decay to high-energy gamma rays and neutrinos.

While the notion of particle acceleration by supernova shocks provides a credible and largely consistent picture, not all observations neatly fit this scheme. Alternative sites for cosmic-ray acceleration may emerge from a detailed study of the neutrino sky. For example, Galactic microquasars, a subclass of X-ray binary systems that exhibit relativistic radio jets, have been identified as possible sources of high-energy neutrino emission (Levinson & Waxman 2001) and potential sources of the highest energy cosmic rays. If they accelerate cosmic rays to high energies, then their dense environment creates suitable conditions for an efficient beam dump.

Turning to extragalactic sources, active galactic nuclei (AGNs) are among the most luminous objects in the universe and promising sources of neutrinos. In these models, high-energy neutrino fluxes are generated near the central engine or in the jets of radio-loud AGNs (e.g., blazars, a class of objects where the jet intersects the line of sight of the observer). The fact that gamma-ray emission has been detected (Catanese & Weekes 1999) from nearby blazars Mrk 421 and Mrk 501 provides strong evidence for particle acceleration to high energies.²⁴ The time-averaged energy spectrum from Mrk 501 during 1997 is consistent with an unbroken power-law energy spectrum up to 10 TeV (Weekes 2001; Konopelko et al. 1999). Beam dump models of neutrino production predict comparable fluxes of gamma-ray photons and neutrinos. However, gamma-ray photons at TeV energies may interact with material or photon fields in the source or interact with the diffuse infrared background photons during their flight. Because of this reprocessing, the measured energy spectrum for gamma-ray photons may not trace the energy spectrum of the source. Consequently, it is possible for the ratio of neutrino flux to gamma-ray flux from a given source to exceed unity. Constraints on this ratio are discussed in § 7.

Recently, it has been argued (Buckley et al. 1998a, 1998b) that the rapid time variability of high-energy photon

²¹ Although the flux limits reported in this paper are computed assuming continuous emission, upper bounds could be generated for periodic or episodic emission as well.

²² Available at <http://area51.berkeley.edu/manuscripts/20010604xx-diffuse-sens.pdf>.

²³ Available at <http://area51.berkeley.edu/manuscripts/20010606xx-grbdoc.pdf>.

²⁴ The review by Catanese & Weekes (1999) presents a current list of detected very high energy gamma-ray sources.

emission from AGN blazars and the correlated variation between the X-ray and TeV regimes disfavor hadronic acceleration models for this particular class of objects, but others have shown that rapid and correlated variability can be accommodated by modest extensions to the existing hadronic acceleration models (Rachen 2000; Dermer 1999). The vigorous debate suggests that high-energy neutrino detectors can play a central role in deciphering the acceleration mechanism.

Figure 1 provides a survey of model predictions for fluxes of high-energy neutrinos. The models were selected to highlight the variation in spectral characteristics. The line labeled 3C 273 is representative of several recent neutrino flux predictions, e.g., a similar differential flux is predicted for microquasars (Distefano et al. 2002) in the region of sky visible to AMANDA and the flat-spectrum radio quasar 3C 279 (Dermer & Atoyan 2001). The figure also shows the differential neutrino flux limit for an assumed source spectrum proportional to E^{-2} for AMANDA-B10 and the anticipated corresponding sensitivity of AMANDA-II and IceCube (Karle et al. 2003). The AMANDA-B10 result, the subject of this paper, is valid for declinations greater than $+40^\circ$. Many theoretical models of potential astronomical neutrino sources predict a very hard energy spectrum, approximately E^{-2} (Learned & Mannheim 2000), which leads to a most probable energy for a detected neutrino well above 1 TeV (typically 10–30 TeV). This high energy is a consequence of three facts: the neutrino cross section for weak interactions increases with neutrino energy, and the propagation length of the secondary muon increases and the

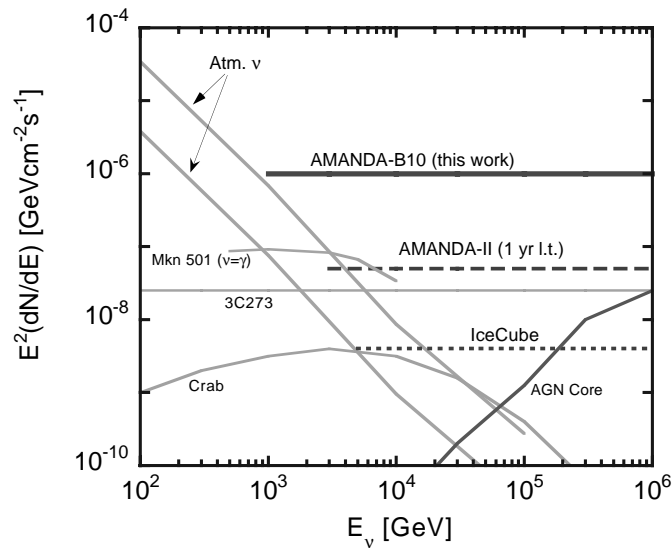


FIG. 1.—Representative survey of $\nu + \bar{\nu}$ flux predictions from cosmic accelerators of high-energy neutrinos. The AMANDA-B10 result is presented here. The dashed horizontal lines give preliminary estimates of the minimum detectable flux by AMANDA-II after 1 yr of live time (Barwick et al. 2001) and IceCube (Spiering 2001). The atmospheric neutrino fluxes (Agrawal et al. 1996) are appropriate for a circular patch of 1° (lower curve) and 3° radius. The curves do not include the normalization uncertainty, possibly 30% in magnitude (Gaisser 2002; T. K. Gaisser 2002, private communication). Models: 3C 273 (Nellen, Mannheim, & Biermann 1993), Crab model I (Bednarek & Protheroe 1999), AGN core (Stecker & Salamon 1996), and Mrk 501 assuming neutrino spectrum is identical to observed gamma spectrum during flaring phase (Weekes 2001). [See the electronic edition of the Journal for a color version of this figure.]

effective detection area increases as light emission along the muon track increases with energy.

Even though the cosmic-ray puzzle provides a powerful motivation to explore the sky for neutrino emission, not all high-energy neutrino sources need to contribute to the cosmic-ray flux. In particular, a powerful accelerator may be surrounded by too much material to emit high-energy photons or cosmic rays (they would interact and cascade down to lower energies), but this accelerator could be discovered by exploiting the neutrino messenger. Several models of such “hidden” sources have appeared in the literature. For example, the predicted flux of neutrinos from pre-AGN objects (Berezinsky & Dokuchaev 2001) leads to a muon detection rate of $\sim 10 \text{ yr}^{-1} \text{ km}^{-2}$.

3. DESCRIPTION OF THE AMANDA DETECTOR

The AMANDA telescope is located below the surface of the Antarctic ice sheet at the geographic South Pole. The neutrino detection technique relies on the detection of Cerenkov light from upward-traveling neutrino-induced muons. Figure 2 shows the current configuration of the AMANDA detector. The shallow array, AMANDA-A, was deployed to depths between 800 and 1000 m in an exploratory phase of the project. The deeper array of 10 strings, referred to as AMANDA-B10, was deployed during the austral summers between 1995 and 1997, to depths between 1500 and 2000 m. At this depth, the optical properties are suitable for track reconstruction (Woschnagg et al.

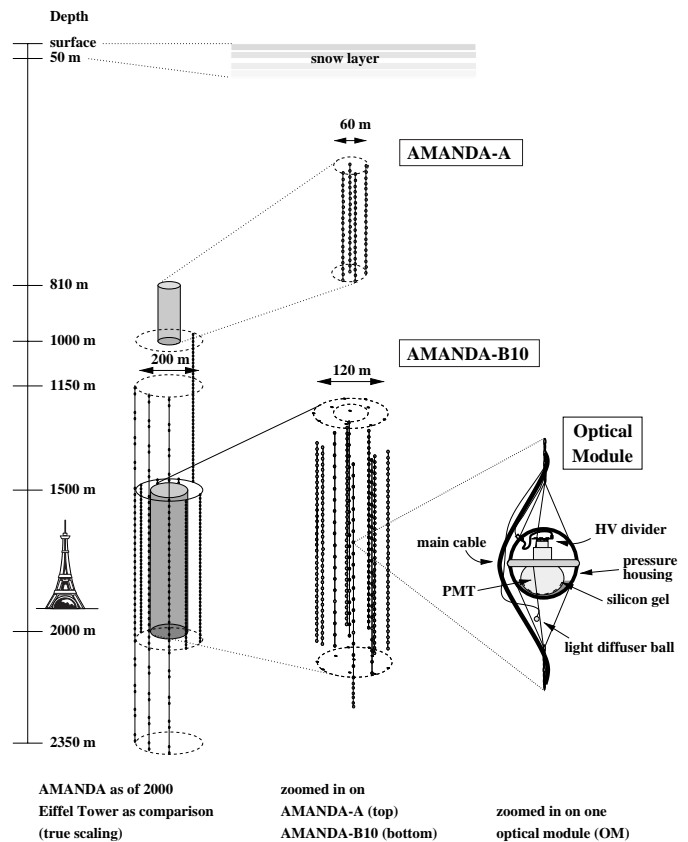


FIG. 2.—Schematic view of the AMANDA neutrino telescope. This paper describes an analysis of data taken in 1997 with AMANDA-B10, the 10 inner strings shown in the expanded view in the center. Each dot represents one optical module in the array. [See the electronic edition of the Journal for a color version of this figure.]

1999).²⁵ The strings are arranged in a circular pattern when viewed from the surface. The instrumented volume of AMANDA-B10 forms a vertical cylinder with a diameter of 120 m. Most electronics are housed on the surface in a research facility located within a kilometer of the Amundsen-Scott South Pole Station. The detector was commissioned in 1997 February (Wischniewski et al. 1999; Barwick et al. 2000) and expanded by adding nine strings of optical modules (OMs) between 1997 December and 2000 January. The composite array of 19 strings forms the AMANDA-II array, which was commissioned in 2000 February.

AMANDA-B10 consists of 302 OMs arranged on 10 vertical strings. Each OM contains an 8 inch (21 cm) diameter photomultiplier tube (PMT) controlled by passive electronics and housed in a glass pressure vessel. The OMs are connected to the surface by dedicated electrical cables, which supply high voltage and carry the anode signals from the PMTs. For each event, the amplitudes and arrival times of the pulses from the OMs are digitized by peak analog-to-digital converter and time-to-digital converter (TDC) values. The TDCs are capable of measuring eight distinct pulses per channel. The precision of the arrival time measurement is 5 ns. Details of deployment, timing resolution, and detector operation can be found in Andres et al. (2000, 2001). Readout of the entire array was triggered by a majority logic system, which demanded that at least 16 OMs produce signals, or “hits,” within a time window of 2.2 μ s. This window takes into account the rather large time variation introduced by the large geometric size of the detector and the cable propagation delays. Random signals from the OMs (or “noise”) were observed at a rate of 300 Hz on the inner four strings and 1.5 kHz for OMs on the outer six strings, the difference being due to different levels of radioactive potassium in the glass pressure vessels. On average, random noise contributed one count per event to the majority trigger.

Optical absorption and scattering properties of the glacial ice that encapsulates the AMANDA detector have been studied using light sources buried with the strings and Cerenkov light from atmospheric muons. These studies (Woschnagg et al. 1999) confirm that the ice is not homogeneous but consists of horizontal strata correlated with climatological events in the past, such as ice ages.²⁶ Variations in the concentration of insoluble impurities between the strata produce a strong modulation of the optical properties. The absorption length, averaged over depth within the AMANDA-B10 array, is 110 m at a wavelength of 400 nm, and the average effective scattering length is approximately 20 m.

The detection of neutrinos relies on the observation of Cerenkov photons generated by muons created in charged-current interactions. At the energies of interest, muons typically propagate for distances in excess of several kilometers (e.g., a muon with $E = 10$ TeV will travel 8 km in water). Therefore, neutrino interactions outside the instrumented volume can be inferred by the presence of a muon, providing a method to extend the volume of the detector beyond the

instrumented boundary of the array. The average angle between the muon direction and the parent neutrino direction, $\langle\theta_{\nu\mu}\rangle$, is approximately $0.65/(E_{\nu}/\text{TeV})^{0.48}$ for E_{ν} less than 100 TeV (Oppelt 2001).²⁷ However, nearly independent of the muon energy, the precision of the measured muon direction in AMANDA-B10 is approximately 4° (see § 6), which dominates the angular uncertainty in the neutrino direction.

The AMANDA-B10 data analyzed here were collected between 1997 April and October. Once construction was completed in 1997 February, calibration and data management activities continued until April. Operations ceased between 1997 late October and 1998 February, because of the beginning of construction of the AMANDA-II array. Furthermore, limitations in the data acquisition and archiving system during that first year of operation reduced the total live time to approximately 130.1 days.

4. SIMULATIONS

Astronomical signals are unlikely to produce more than a few tens of upgoing neutrino events per year in AMANDA-B10. Data are therefore overwhelmingly dominated by two types of background: downgoing atmospheric muons generate essentially all of the recorded events, and atmospheric neutrinos contribute a few tens of events per day. The point-source search relies on a good understanding of both signal and background through simulations based on Monte Carlo techniques.

Atmospheric muon events are generated from the measured flux of cosmic rays (Wiebel-Sooth & Biermann 1998). Two different air shower simulation packages were used to assess systematic uncertainty: BASIEV (Bosiev et al. 1989) and CORSIKA (Version 5.6; Heck et al. 1998, 1999) using the QGSJET hadronic interaction model. CORSIKA was modified to include the curved geometry of the Earth and atmosphere to provide a more accurate description of the flux at zenith angles close to the horizon. Most characteristics of the events generated with BASIEV were found to be similar to those from the more accurate but computationally more intensive CORSIKA simulation. The density profile of the atmosphere was modified for polar conditions, but no attempt was made to replicate the small seasonal variations of the trigger rate (Bouchta et al. 1999).²⁸ Muon tracking from the surface to the detector was handled by the muon propagation program MUDEDX (Lohmann, Kopp, & Voss 1985; W. Lohmann, R. Kopp, & R. Voss 1995, private communication [MUDEDX Version 2.02]), and the energy-loss characteristics were compared against two additional propagation programs that are available for general use: PROPMU (Lipari & Stanev 1991) and MMC (Rhode & Chirkin 2001). Integral lateral distributions of muons at the depth of AMANDA were simulated for proton and iron showers (X. Bai et al. 2003, in preparation) and used for verification of the detector performance as described below.

The propagation of upward-traveling muons from neutrino interactions was treated differently from that of downgoing atmospheric muons because the energies of signal neutrinos were expected to extend to much higher energies.

²⁵ Available at http://krusty.physics.utah.edu/~icrc1999/root/vol2/h4_1_15.pdf.

²⁶ See P. B. Price, K. Woschnagg, & D. Chirkin (2000), AMANDA public manuscript 20000201, available at <http://amanda.berkeley.edu/manuscripts>.

²⁷ Available at <http://www-zeuthen.desy.de/~apohl/files/doktor/ps.gz>.

²⁸ Available at http://krusty.physics.utah.edu/~icrc1999/root/vol2/h3_2_11.pdf.

Neutrinos were tracked through the Earth and allowed to interact in the ice within or near the instrumented volume of the detector or in the bedrock below (Hill 1997). Muons with energies above $10^{5.5}$ GeV at production were propagated using PROMMU until they reached the rock-ice boundary and then propagated through the ice in exactly the same way as downgoing atmospheric muons. For energies below $10^{5.5}$ GeV at the production vertex, muons were tracked with MUDEDX. The background fluxes from atmospheric ν_μ and $\bar{\nu}_\mu$ (Agrawal et al. 1996) were included (AMANDA cannot differentiate the charge sign of the muon).

In addition to background from atmospheric muons and muon neutrinos, the detection efficiency for atmospheric electron neutrinos has been simulated. At the relevant energies, the flux of ν_e is far smaller than for ν_μ , so the background contribution is small a priori. Furthermore, the topology of electron neutrino events, reflecting the electromagnetic shower generated by the secondary electron, is spherical rather than linear, and this characteristic has been exploited to further increase the rejection. Simulations show that the detection rate of atmospheric ν_e in the point-source analysis is only 0.3% of ν_μ (Young 2001)²⁹ and therefore negligible in this context. We note that a separate analysis was devised to search for electron neutrinos and consequently achieved a much larger sensitivity (Ahrens et al. 2002c).

An overview of the simulation of the detector response is given in Hundertmark (1999). The depth dependence of the optical properties of the bulk ice (Woschnagg et al. 1999)³⁰ is included along with a realistic treatment of trigger conditions, intrinsic noise rates, and hardware-dependent pulse shapes. The linearity and saturation of the photomultiplier response is included. The angle-dependent sensitivity of the optical module was computed from a convolution of PMT quantum and collection efficiencies as estimated by the manufacturer, detection efficiency, wavelength-dependent transparency through the pressure housing and buffer gel, and obscuration by cables and mechanical support hardware. The relative angular dependence of the sensitivity of the photomultiplier tubes was measured in the laboratory. The local optical properties of the refrozen ice were included in the photon tables that describe the probability and the timing characteristics of photon propagation (Ahrens et al. 2002a).

Figure 3 presents the differential distribution of the multiplicity of optical modules, or channels, participating in an event, N_{ch} , for the full detector simulation and for experimental data after known detector-related artifacts were removed. The integrated rates differ by less than 25%, which is within the systematic uncertainties associated with the flux of the primary cosmic rays (Gaisser 2002; T. K. Gaisser 2002, private communication) and uncertainties associated with the absolute sensitivity of the optical module (see § 8). The agreement in the shape of the distribution demonstrates a good understanding of the overall sensitivity of the array for the most common events that trigger AMANDA-B10.

As the inset of Figure 3 shows, the largest values of N_{ch} are produced by events with more than one muon. This

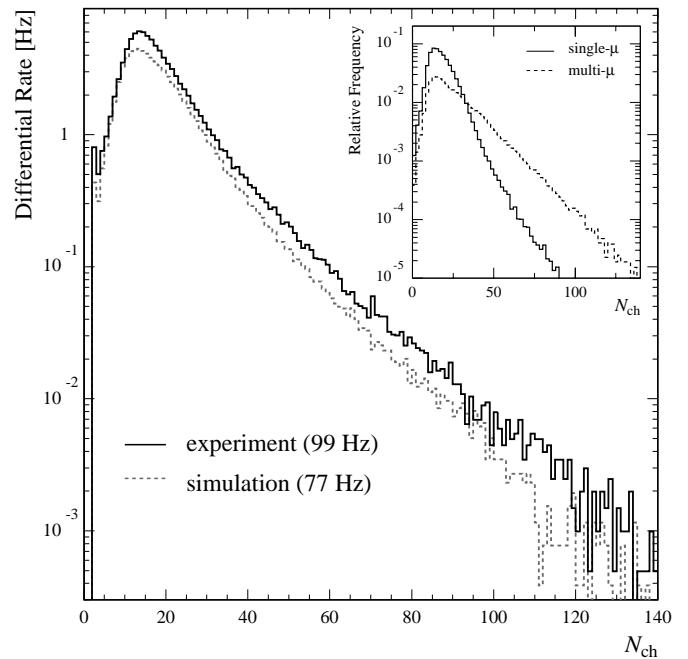


FIG. 3.—Differential distribution of observed (*solid curve*) and predicted (*dashed curve*) trigger rates as a function of the event multiplicity N_{ch} (i.e., the number of optical modules that participate in each event). The integrated rates are given in parentheses. Note that N_{ch} extends below the majority logic threshold of 16 because of removal of data caused by experimental artifacts. *Inset*: Relative contribution to the trigger rates from single muons (*solid curve*) and multiple-muon bundles (*dashed curve*) that traverse the fiducial volume of the array. [See the electronic edition of the Journal for a color version of this figure.]

information provides indirect evidence that the response of AMANDA to single high-energy muons is correctly modeled, by the following argument. MultimMuon bundles that reach AMANDA mainly consist of muons below the critical energy of 600 GeV, which implies that energy loss due to ionization is near minimum. The Cerenkov light production from muons well above the critical energy is dominated by electromagnetic showers, and the total light from a muon with E_μ is approximately equal to the light of a bundle of N muons, where $N \sim E_\mu/E_{\text{crit}}$. Therefore, the light production by a multimMuon event can be related to the light production by a single-muon event. For example, the average energy loss per unit length for a muon with energy 10^{13} eV is approximately a factor of 15 larger than for a single muon, as long as the energy is below 600 GeV. There are several modest limitations to this line of reasoning. One is that the lateral distribution of multimMuon events generates Cerenkov photons over a much larger cylinder than a single muon. Another difference is that multimMuon events deposit Cerenkov photons more uniformly than the equivalent high-energy muon, for which energy loss is dominated by occasional pair production and bremsstrahlung. However, optical scattering by the ice mitigates the effects of nonuniform photon generation. Simulations show that bundles of 20 muons generate an N_{ch} distribution similar to that of single muons with an energy of 10 TeV. The correlation between muon multiplicity and N_{ch} multiplicity is shown in Figure 4. Note that bias introduced by the majority logic in the trigger prevents the muon multiplicity from converging to zero as N_{ch} approaches zero.

²⁹ Available at <http://area51.berkeley.edu/manuscripts/20010702xx-young-main.pdf>.

³⁰ Available at <http://krusty.physics.utah.edu/~icrc1999/proceedings.html>.

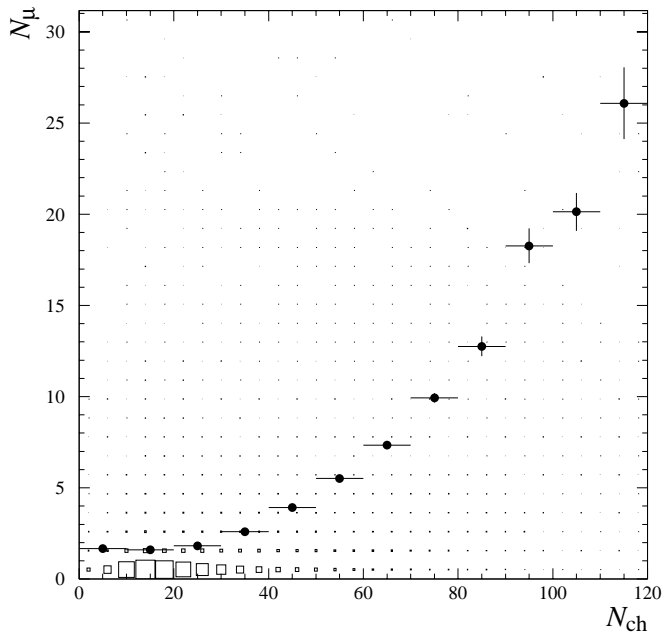


FIG. 4.—Muon multiplicity N_μ vs. OM multiplicity N_{ch} from a full detector simulation. The area of the boxes is linearly proportional to number of events. The average values (dots) show the correlation between these two quantities, and the vertical error bars show the statistical uncertainty.

5. ANALYSIS PROCEDURE

The analysis procedure exploits two essential characteristics of the signal to simplify the analysis relative to atmospheric neutrino measurements. First, the sources are assumed to be point sources in the sky, so only events within a restricted angular region are considered. Second, we use the topological and directional characteristics of the spectrally hard neutrino signal to help reject poorly reconstructed atmospheric muons (i.e., downward-traveling muons reconstructed as upward traveling) and atmospheric neutrinos, both of which have softer spectra. Unlike many neutrino detectors, the effective sensitivity of AMANDA varies dramatically as a function of the background-rejection requirements. By concentrating on harder spectra, the effective area of the detector can be increased by relaxing the background-rejection criteria. Since the point-source analysis tolerates a larger background (B) contamination in the final data sample, the analysis procedure optimizes on signal to noise (S/\sqrt{B}) rather than signal purity (S/B).

Prior to track reconstruction and event selection, experimental data were selected from runs that exhibited no abnormal behavior, and various instrumentally induced artifacts were removed. Once the data in the runs were certified, individual OMs in the array were examined to insure proper operation. OM channels with hardware malfunction ($\sim 15\%$ of OMs), such as pickup from unusually large external noise sources or fluctuations in the response of the amplifier electronics, were rejected. Approximately 85% of OMs remained after deselection. Occasional signals induced by cross talk in the electrical cables or surface electronics exhibited characteristic behavior and could be removed by straightforward restrictions on pulse amplitude and width. Noise signals generated internally by the photomultiplier tubes were readily removed if their time of arrival occurred earlier than 5 ms prior to the formation of the event trigger.

The reconstruction programs stochastically account for PMT noise within the event duration.

After this initial data cleaning, a number of event reconstruction techniques (Andres et al. 2000) are applied to the data. The most sophisticated technique relies on a search in multiparameter space to find the maximum likelihood for a track hypothesis given the recorded hits. After reconstruction is completed, events are selected according to a set of criteria that retain only the highest quality events that possess topological and directional information consistent with those expected for upgoing neutrino-induced muons. In a first step, the data sample of 1.05×10^9 events at trigger level is reduced to a more manageable size by two filtering stages. Most events in data are readily identified as due to downward-traveling muons by computationally fast reconstruction routines. Removing these events reduces the data approximately by a factor of 10^3 .

An iterative analysis procedure was developed to maximize S/\sqrt{B} for a simulated signal with an energy spectrum proportional to E^{-2} . It ignored the absolute time of the event, which helped to minimize bias from potential sources in the data. In this optimization the background was determined from experimental data by assuming that the fraction of signal events in the data sample is negligible. After the filtering stages, cuts were applied sequentially on a set of selection variables, with several variables included more than once. The specific value for each cut after stage 2 was chosen to retain $\gtrsim 80\%$ of the signal. At each stage, given this constraint on signal efficiency, the same cut was made on data for the variable with the largest rejection power, $R = \epsilon_{sig}/\epsilon_{bgr}$, where $\epsilon = N^{pass}/N^0$, and N^0 and N^{pass} are the numbers of events before and after the application of the selection cut, respectively. The signal-to-noise ratio was then computed as a function of zenith angle to ensure that the acceptance of AMANDA-B10 remained as large as possible near the horizon. The effective areas for detection of background and signal needed for this computation were determined from simulations (as described in § 7). After each stage, this procedure was repeated on the remaining variables.

Besides restrictions on the reconstructed zenith angle θ , the most effective selection criteria impose a threshold on the number N_{dir} of only slightly scattered, or “direct,” photons (i.e., photons that travel between the reconstructed track and the OM in nearly a straight line) and the track length L_{dir} over which these photons are detected. Furthermore, the analysis requires a minimum goodness-of-fit value from the maximum likelihood procedure. Other criteria evaluate the topological distribution of the photon emission using variables that describe the granularity of the light pattern along the trajectory and a related observable that assesses the sphericity of the photon pattern.³¹ Table 1 shows the selection variables and cuts used in this analysis, including a brief technical description of the two filtering stages. The selection variables were introduced previously (Ahrens et al. 2002a), and a complete description is also available (Young 2001). Also shown in the table are efficiencies and rejection factors at each stage of the analysis for experimental data, simulated background, and simulated signal, averaged over all angles.

³¹ Muons normally generate a linear distribution of Cerenkov photons, whereas electromagnetic cascades initiated by pair production or bremsstrahlung produce spherically symmetric distributions.

TABLE 1
DESCRIPTION OF VARIABLES USED IN ANALYSIS

Stage	Selection Cut	ϵ_{data}	ϵ_{bgr}	ϵ_{sig}	R_{data}	R_{bgr}
0.....	Trigger	1	1	1
1.....	Filter 1:	0.0193	0.0190	0.433	22.4	22.8
1a.....	$\theta^{(1)} > 50^\circ$
1b.....	$\theta^{(2)} > 80^\circ$
1c.....	$N_{\text{dir}(b)}^{(2)} > 2$
2.....	Filter 2:	0.0232	0.0283	0.538	23.2	19.0
2a.....	$\theta^{(2)} > 90^\circ$
2b.....	$-0.43 < S_{\text{mrl}}^{(2)} < 0.3$
2c.....	$L_{\text{dir}(c)}^{(2)} > 75 \text{ m}$
2d.....	$\mathcal{L}^{(2)} / \mathcal{L}^{(1)} < 4 \times 10^{-6}$
2e.....	$\theta^{(5)} > 90^\circ$
3.....	$\cos \theta^{(5)} < -0.1$	0.867	0.861	0.925	1.07	1.07
4.....	$\mathcal{P}_{\text{up}}^{(5)} / \mathcal{P}_{\text{down}}^{(5)} > 9.2$	0.212	0.178	0.817	3.85	4.59
5.....	$\mathcal{L}^{(5)} / \mathcal{L}^{(4)} < 1.02$	0.370	0.334	0.947	2.56	2.84
6.....	$-0.21 < S_{\text{phit}}^{(3)} < 0.33$	0.458	0.408	0.927	2.02	2.27
7.....	$L_{\text{dir}(c)}^{(5)} > 100 \text{ m}$	0.638	0.657	0.932	1.46	1.42
8.....	$N_{\text{dir}(c)}^{(5)} - N_{\text{dir}(c)}^{(4)} > 3$	0.737	0.710	0.912	1.24	1.28
9.....	$-0.25 < S_{\text{mrl}}^{(5)} < 0.26$	0.711	0.671	0.912	1.28	1.36
10.....	$L_{\text{dir}(b)}^{(5)} > 40 \text{ m}$	0.744	0.698	0.955	1.28	1.37
11.....	$\mathcal{P}^{(5)} / \mathcal{P}^{(4)} > 9.2$	0.581	0.562	0.921	1.59	1.64
12.....	$\mathcal{L}^{(3)} < 4.9$	0.515	0.466	0.906	1.76	1.94
13.....	$N_{\text{dir}(c)}^{(5)} > 9$	0.659	0.616	0.963	1.46	1.56

NOTES.—Description of selection criteria applied to reconstruction variables in the data reduction procedure. For additional information on the filters and selection variables, consult Young (2001). The numerical identification (superscript in parentheses) refers to the reconstruction algorithm of the event: (1) line fit used as first guess for likelihood fit; (2) maximum likelihood method for muon track; (3) hit probability reconstruction based on radial distribution of OMs that detect photons; (4) maximum likelihood method assuming cascade event; (5) iterative application of maximum likelihood for muon track. Direct hits are photons that arrive within (b) $[-15, +25]$ ns or (c) $[-15, +75]$ ns of the unscattered time of flight between track and optical module. The reduced likelihood parameter \mathcal{L} is $-\log(\mathcal{P})$ divided by the number of degrees of freedom, where \mathcal{P} is the maximized probability. Passing efficiencies (ϵ) relative to the prior stage are shown at each stage for experimental data, simulated background, and simulated signal. Rejection factors (R) for experimental data and simulated background are shown for each stage in the two columns farthest to the right.

The simulated background from atmospheric muons and neutrinos is compared to data at all stages of the analysis to establish confidence in the simulation. Figure 5 shows the comparison at stage 4, which is sufficiently early in the analysis to retain high statistical precision. All distributions are equally normalized because the optimized cut value depends on the fraction of events that remain (*bottom panel*). Figure 6 shows the final stage (13) of the analysis procedure. We note that the signal sensitivity determined from simulations is quite robust against small deviations between the simulated event distribution and the actual response of the detector (Young 2001).

Because of the large experimental data sample, precision studies of detector performance are possible from the most common events in the sample to extremely rare components. The predicted and experimental sample sizes are compared through all stages of the analysis to establish the absolute calibration of detector sensitivity. This method assumes that signal from astronomical sources contributes negligibly to the sample. Figure 7 shows that the simulated background and data agree to within a factor of 2 at all

stages of the analysis even though the size of the event samples varies by 6 orders of magnitude. The relative rates and the agreements in shape of the selection variable distributions provide evidence that the background generators and detector simulation programs are an adequate description of the detector physics, including detector response. Because of the optimization on signal to noise, all stages of the analysis produce event samples that are dominated by poorly reconstructed downgoing atmospheric muon events. Diffuse backgrounds from atmospheric neutrinos become noticeable only after rejecting most of the poorly reconstructed atmospheric muons, but they never dominate the event sample.

Obviously, atmospheric muon data are an imperfect tool to investigate the sensitivity of the detector to neutrino-induced muons, because of the downgoing nature of the events and differences in the energy and multiplicity distributions. This concern is addressed by the measurement of atmospheric neutrinos (Andres et al. 2001; Ahrens et al. 2002a), which were used to verify the basic operational sensitivity of AMANDA-B10 to a known neutrino signal. In

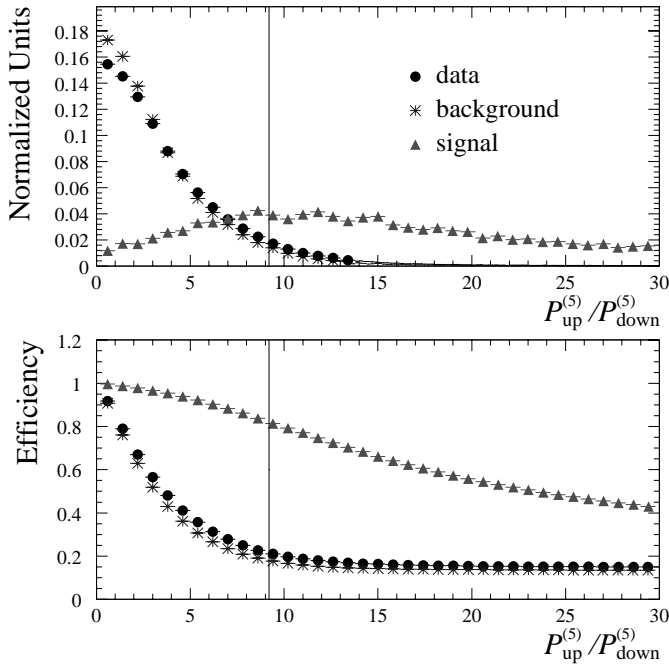


FIG. 5.—*Top*: Equally normalized distributions for experimental data (circles) and simulated background (asterisks) and signal (triangles) for stage 4 of the point-source analysis, which compares the best likelihood for an upgoing track hypothesis with the likelihood for a track in the opposite (i.e., downgoing) direction. *Bottom*: Passing efficiencies as a function of cut value. The efficiency is obtained from the integrated sums of distributions shown in the top panel from given value to infinity. The vertical lines indicate the cut applied in the analysis. [See the electronic edition of the Journal for a color version of this figure.]

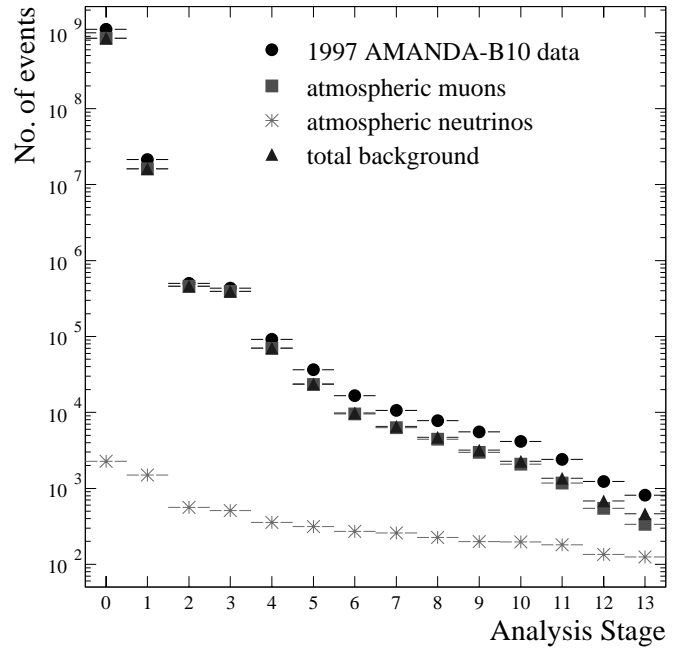


FIG. 7.—Number of events remaining in the sample as the selection criteria in the 13 analysis stages listed in Table 1 are applied sequentially. The 1997 AMANDA-B10 data (circles) are compared to simulated background from atmospheric muons generated by cosmic-ray interactions (squares) and from muons induced by atmospheric neutrinos (asterisks). Also shown is the sum of atmospheric muon and neutrino backgrounds (triangles). No normalization was applied, but systematic uncertainty at the trigger level (analysis stage 0) may be as large as $\pm 30\%$. [See the electronic edition of the Journal for a color version of this figure.]

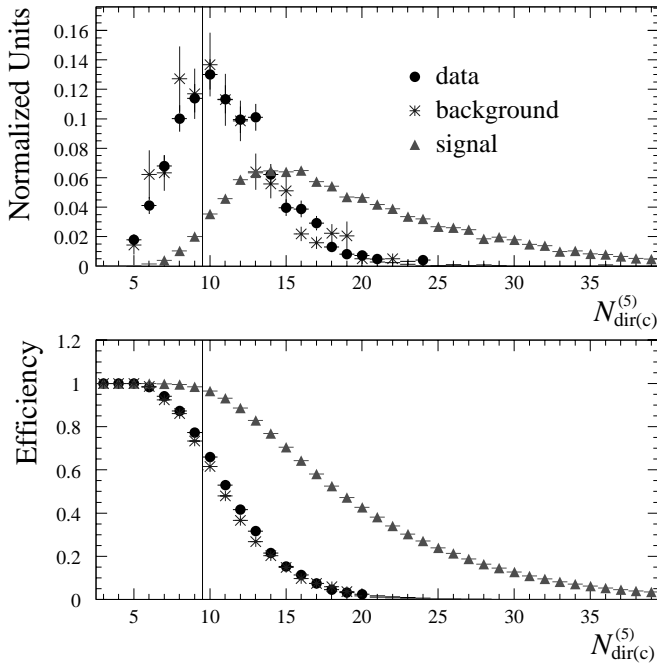


FIG. 6.—*Top*: Similar to Fig. 5, but for analysis stage 13, which involves the number of direct hits in a time window of -15 to $+75$ ns. *Bottom*: Passing efficiencies—defined as integrated sums, from given value to infinity, of distributions shown in the top panel—as a function of cut value. The vertical lines indicate the cut applied in the analysis. [See the electronic edition of the Journal for a color version of this figure.]

this analysis, the relative agreement between the measured and predicted event rates is 30%, which is consistent with uncertainties in the measured flux of cosmic-ray primaries, theoretical uncertainty in the interaction models, and systematic uncertainties in the modeling of the detector response. However, because of the steeply falling energy spectrum for atmospheric neutrinos, the mean energy of the muons induced by charged-current interactions is close to the energy threshold of the detector, which implies that they cannot be used to reliably probe the high-energy response of AMANDA-B10.

6. POINTING RESOLUTION AND POINT-SOURCE SEARCH

The final stage of the data analysis procedure yields a sample of 815 events (as is evident from Fig. 7, atmospheric neutrinos contribute about 25% of the events to the simulated background). Visual inspection of the distribution in the sky of the final event sample, shown in Figure 8, reveals no obvious clustering. The increase in event density near the horizon (decl. = 0°) is due to the zenith dependence of the atmospheric muon component of the background. In order to perform a quantitative search for possible sources of high-energy neutrinos in the northern hemisphere, the sky was divided into nonoverlapping angular bins of approximately equal solid-angle coverage. A point source would then be revealed by a statistically significant clustering of events within a particular angular bin. The optimal bin size and shape depend on the space-angle resolution of the detector, which can be expressed in terms of a point-spread function. The space-angle deviation Ψ between the true

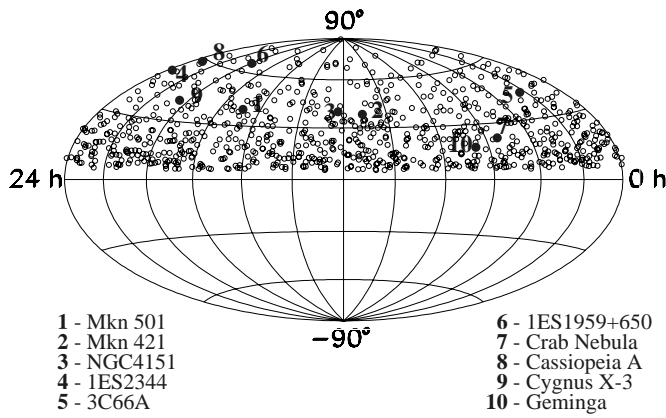


FIG. 8.—Sky plot of 815 events obtained from the point-source analysis. Horizontal coordinates are right ascension, and vertical coordinates are declination. Also shown are the sky coordinates for 10 potential high-energy neutrino sources. [See the electronic edition of the *Journal* for a color version of this figure.]

angular coordinates of a muon ($\theta_{\text{true}}, \phi_{\text{true}}$) and the reconstructed coordinates ($\theta_{\text{rec}}, \phi_{\text{rec}}$) is given by

$$\cos \Psi = \cos \theta_{\text{rec}} \cos \theta_{\text{true}} + \sin \theta_{\text{rec}} \sin \theta_{\text{true}} \cos(\phi_{\text{rec}} - \phi_{\text{true}}). \quad (1)$$

Figure 9 shows the distribution of Ψ and the corresponding point-spread function, computed from the Ψ -distribution by dividing by the appropriate solid angle, for the simulated sample of upward-traveling muons generated by neutrinos with an E^{-2} energy spectrum. A median value of $\Psi = 3.9^\circ$, averaged over positive declinations, is achieved. A function involving the sum of two Gaussian distributions was fitted to the point-spread function. It yields an amplitude ratio of

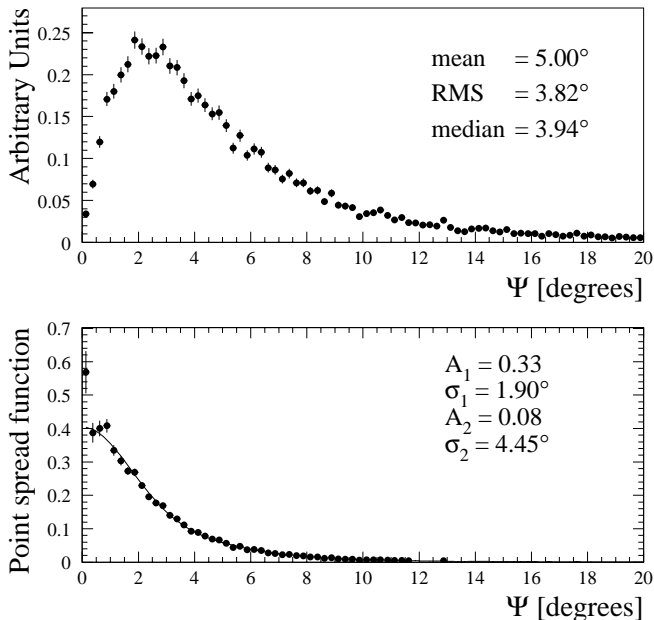


FIG. 9.—*Top*: Distribution of space angle Ψ between true and reconstructed muon track direction for simulated signal with neutrino energy spectrum proportional to E^{-2} , averaged over direction. *Bottom*: Point-spread function for signal in AMANDA-B10, deduced from the space-angle distribution in the top panel. A function composed of the sum of two Gaussians was used to characterize this distribution.

$A_2/A_1 = 0.25$, indicating the importance of the second component related to the degrading angular resolution at large muon energies (Young 2001). Given this point-spread function and the relatively small number of background events shown in Figure 8, the optimal slice in zenith angle is 11.25° (Young 2001). For azimuth angle, a weak optimum occurs for a width of 12° for the declination band closest to the horizon. These angular dimensions of the bins were chosen to maximize the signal to noise.

Two studies were performed to check the predicted space-angle resolution and absolute pointing accuracy. The first uses AMANDA events that were also tagged by the GASP air Cerenkov telescope (Barbagli et al. 1993). GASP determines the direction of the air shower, and AMANDA measures the direction of the penetrating muon component. At AMANDA depths, these events are almost entirely single muons. Unfortunately, the duty cycle of operation is low, so the sample size is relatively small. To improve the statistical accuracy of the angular resolution studies, a second method based on extensive air showers was developed. This method utilized events that triggered both the SPASE array and AMANDA (X. Bai et al. 2003, in preparation). SPASE responds to the electron and photon content of the shower front that reaches the surface. Since the direction of muons within the air shower event is nearly perpendicular to the shower front, the difference between the direction of the air shower and the reconstructed muon direction can be used to deduce the angular resolution of AMANDA. SPASE measures the direction of an air shower with a pointing resolution of approximately 1° – 2° (Dickinson et al. 2000; depending on shower size), which is small enough to calibrate the AMANDA pointing resolution.

In this study, AMANDA data were analyzed using the procedure outlined in Table 1, with the exception that angle-dependent cuts were inverted to account for the downgoing direction of travel of SPASE/AMANDA coincidence events (e.g., the cut at stage 3 was changed to $\cos \theta^{(5)} > 0.1$). The absolute pointing accuracy is characterized by the average of $\Delta\theta$, the difference between the true and the reconstructed zenith angle. Because of the excellent zenith-angle resolution of SPASE, SPASE/AMANDA coincidence data were used to deduce $\Delta\theta$ using the reconstructed zenith angles of both detectors, $\Delta\theta = \theta_{\text{AMANDA}} - \theta_{\text{SPASE}}$. Figure 10 shows the measured zenith-angle resolution using SPASE/AMANDA coincidence events, together with the resolution obtained for a SPASE/AMANDA simulation of air showers initiated by protons and iron nuclei. Iron primaries produce a larger fraction of coincidence events with more than one muon penetrating to AMANDA depths, which accounts for the small difference between protons and iron nuclei. The coincidence data support the predicted angular resolution and show that the angular offset is small compared to the angular dimensions of the sky bins. These conclusions are nearly independent of the choice of cosmic-ray primary.

Also shown in Figure 10 is the expected angular resolution as function of declination for single muons with energies of 0.1 and 4 TeV within the detector volume. These muon energies were chosen to be representative of the average muon energy that were initiated by atmospheric neutrinos and by a source with a differential energy spectrum proportional to E^{-2} . The predicted value for the absolute offset is less than 1.5° , which is consistent with results obtained by additional study of the SPASE/AMANDA

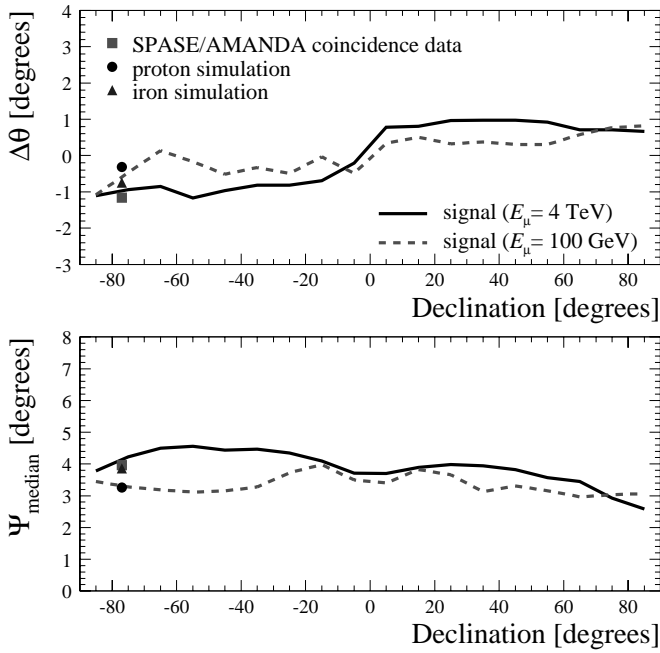


FIG. 10.—Offset in reconstructed zenith angle (*top*) and median space angle (*bottom*) as a function of declination. Positive declination corresponds to upward-traveling events in the AMANDA array. SPASE/AMANDA coincidence data (*squares*) are compared to expectation assuming that the cosmic-ray elemental composition is entirely protons (*circles*) or iron nuclei (*triangles*). Also shown is the expectation for signal (i.e., neutrino-induced muons) with two different energies within the detector. [See the electronic edition of the *Journal* for a color version of this figure.]

and GASP/AMANDA coincidence events (Rawlins 2001; X. Bai et al. 2003, in preparation).³² The offset is due to bias in the AMANDA event reconstruction, which tends to produce more vertical events. This effect is most evident from the high-energy muon simulation, which shows that the angular offset changes sign for positive and negative declinations. Since the absolute offset is substantially smaller than the angular resolution and small compared to the size of the search bin, the offset has minimal impact on the signal efficiency. For a zenith (declination) offset of $1^{\circ}5$, 6% of the signal events are shifted to the neighboring bin. The bottom panel of the figure also shows that the angular resolution for upward-traveling events is slightly better than for events traveling in the downward direction, presumably because of the asymmetry in the response of the photomultiplier tubes, which are oriented toward the center of the Earth.

To obtain approximately equal solid-angle coverage for all bins, the northern sky is divided into 154 nonoverlapping bins, using the calculated optimal declination slice ($11^{\circ}25$) and a varying number of bins in azimuth for the resulting eight declination bands—from 30 near the horizon to three near $+90^{\circ}$ declination. Each angular bin is then tested for an excess of events by computing the significance,

$$\xi = -\log_{10}(P), \quad (2)$$

where

$$P = \sum_{n=N_0}^{\infty} \frac{e^{-\mu} \mu^n}{n!} \quad (3)$$

is the probability of the bin containing at least the observed number of events N_0 , assuming that fluctuations are described by a Poisson distribution. The expected mean number of events μ is obtained by taking the average of the number of events in all other bins in the same declination slice. The polar location of AMANDA assures equal sky coverage for all declinations, independent of time gaps in the collection of data. Figure 11 shows the distribution of significance for the experimental data and for random fluctuation of the background events. This noise estimate is obtained by randomizing the right ascension coordinate of the data events, then recalculating ξ for each bin. A point-source candidate is identified by a large observed value of significance with a large ratio to the significance expected from random fluctuations of background. To avoid the statistical problem of a potential source near a bin boundary distributing signal between two adjacent bins, the procedure was repeated with the grid shifted by one-half of a bin in both declination and azimuth. The largest value of significance, $\xi = 1.85$, appears in the bottom panel. Taking into account the 154 bins in the sky and the two versions of the sky grid, there is a 40% probability that the most significant sky bin is produced by random fluctuation of background. Therefore, the distribution of significance shows no evidence of a source.

Another approach was also investigated, using the angular correlation function between event pairs to avoid the problem of a source near a bin boundary, but this alternate approach did not reveal sources either (Young 2001).

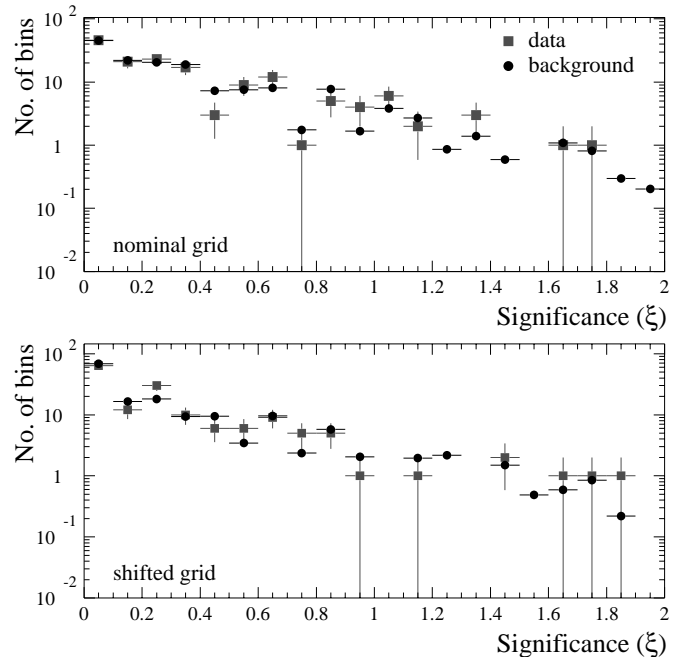


FIG. 11.—Distribution of significance for the 154 sky bins. Data (*squares*) are compared to expectation from randomized background (*circles*). The statistical uncertainty of the randomized background is negligible. The top panel shows the results for the nominal sky grid. The sky grid used in the bottom panel has been shifted from the nominal sky grid by one-half of a bin in both right ascension and declination. [See the electronic edition of the *Journal* for a color version of this figure.]

³² Available at http://area51.berkeley.edu/manuscripts/20011002xx-kaths_thesis.pdf.

7. FLUX LIMITS

The absence of a detected source translates into an upper limit on the high-energy neutrino flux. Neutrino flux and neutrino-induced muon flux limits depend on the effective area of the detector A_{eff} for a muon with energy E_μ . The effective area, obtained by dividing the signal rate by the incident flux, is determined from simulations by

$$A_{\text{eff}}(E_\mu) = f_{\text{ev}}(E_\mu) A_{\text{GEN}}, \quad (4)$$

where A_{GEN} is the cross-sectional area of the cylinder in the simulation that contains all neutrino interaction vertices and f_{ev} is the fraction of generated muon events that survive the 13-stage data analysis procedure. As an example, results are shown in Figure 12 for muon vertices located near the detector. The effective area is computed as a function of declination for muons with energies of 1, 10, and 100 TeV. These effective areas can be contrasted to the geometric cross section of the instrumented volume of deep ice, which spans from $1.1 \times 10^4 \text{ m}^2$ in the vertical direction to $6.1 \times 10^4 \text{ m}^2$ in the horizontal direction.

The *average* effective area, folding in the source spectra, detector response, and the probability of a neutrino-nucleon interaction, is given by

$$\begin{aligned} \bar{A}_{\text{eff}}^i &= N_A \rho_{\text{ice}} A_{\text{GEN}} \left[\int_{E_\nu^{\text{min}}}^{E_\nu^{\text{max}}} \sigma_{\nu\mu}(E_\nu) S(E_\nu) \right. \\ &\quad \times \left. \langle R(E_\nu; E_\mu^{\text{min}}) \rangle f_{\text{ev}} \frac{d\phi_\nu}{dE_\nu} dE_\nu \right] \\ &\quad \times \left(\int_{E_\nu^{\text{min}}}^{E_\nu^{\text{max}}} \frac{d\phi_i}{dE_\nu} dE_\nu \right)^{-1}, \end{aligned} \quad (5)$$

where the index i denotes either μ or ν , and $E_\nu^{\text{min}} = 10 \text{ GeV}$ and $E_\nu^{\text{max}} = 10^7 \text{ GeV}$ define the energy range in the simula-

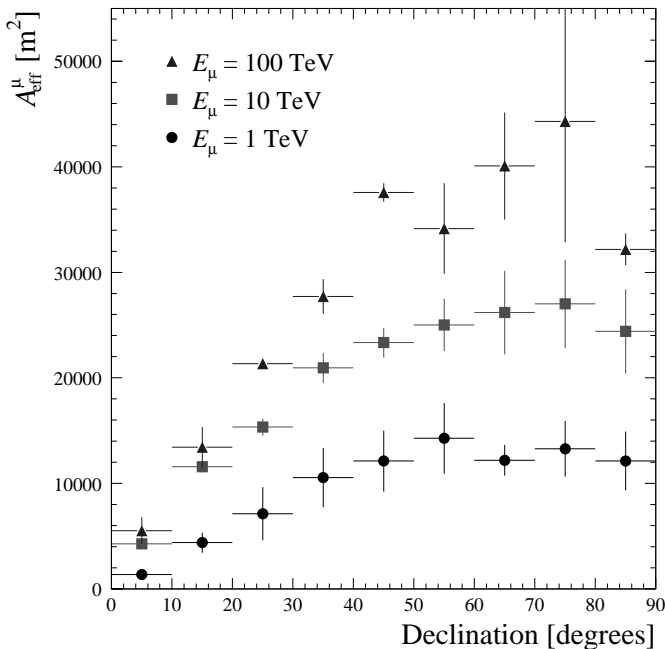


Fig. 12.—AMANDA-B10 effective area for muon detection as a function of declination (90° is vertically up) for three different muon energies at the detector. The vertical error bars are statistical. [See the electronic edition of the Journal for a color version of this figure.]

tion, which safely brackets the interval of interest for most theoretical models. The other variables are N_A , Avogadro's number, ρ_{ice} , the molar density of nucleons in ice, and $\sigma_{\nu\mu}$, the charged-current cross section for ν_μ (or $\bar{\nu}_\mu$) interactions. The term $S(E_\nu)$ accounts for neutrino absorption in the Earth, and $\langle R(E_\nu; E_\mu^{\text{min}}) \rangle$ is the average propagation length for a muon created by a neutrino with energy E_ν , corrected for the energy threshold of the detector. In this calculation, the neutrino interaction vertices are located randomly within a volume that is large compared to the instrumented volume of the detector. The propagation programs properly account for muon energy losses.

The muon differential flux is related to the neutrino differential flux by

$$\frac{d\phi_\mu}{dE_\nu} = \sigma_{\nu\mu}(E_\nu) S(E_\nu) \langle R(E_\nu; E_\mu^{\text{min}}) \rangle \frac{d\phi_\nu}{dE_\nu}. \quad (6)$$

The energy-averaged muon effective area is presented in Figure 13 for different spectral indexes. The energy response of AMANDA is described by the distribution of E_μ at the detector, which depends on the spectral index of the neutrino spectrum. Figure 14 shows the distribution for differential spectra proportional to E^{-2} and E^{-3} . For E^{-2} , the most probable muon energy (mode) is 5 TeV, and the central 90% of the muon events are within the energy interval 80 GeV to 200 TeV. For a spectral index of 3, appropriate for atmospheric neutrinos, the most probable detected energy of the muon is much lower.

If neutrino emission from a point source is described by a differential energy spectrum, the energy-averaged flux limit is calculated from

$$\Phi_i^{\text{limit}} = \frac{\mu_s(N_0, N_{\text{bgr}})}{T_{\text{live}} \epsilon_{\text{bin}} \bar{A}_{\text{eff}}^i}. \quad (7)$$

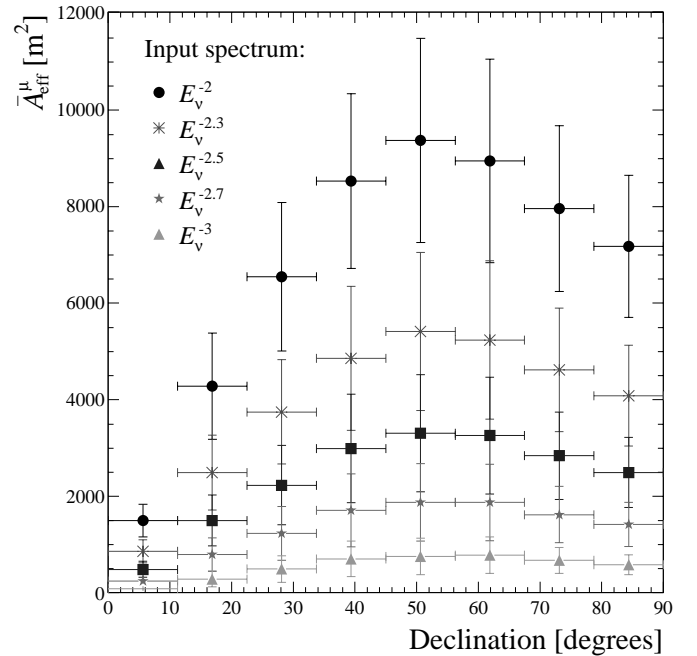


Fig. 13.—AMANDA-B10 average effective area for muon detection as a function of declination (90° is vertically up) for assumed differential neutrino spectral indexes between 2 and 3. The vertical error bars indicate the uncertainty obtained from studies described in § 8. [See the electronic edition of the Journal for a color version of this figure.]

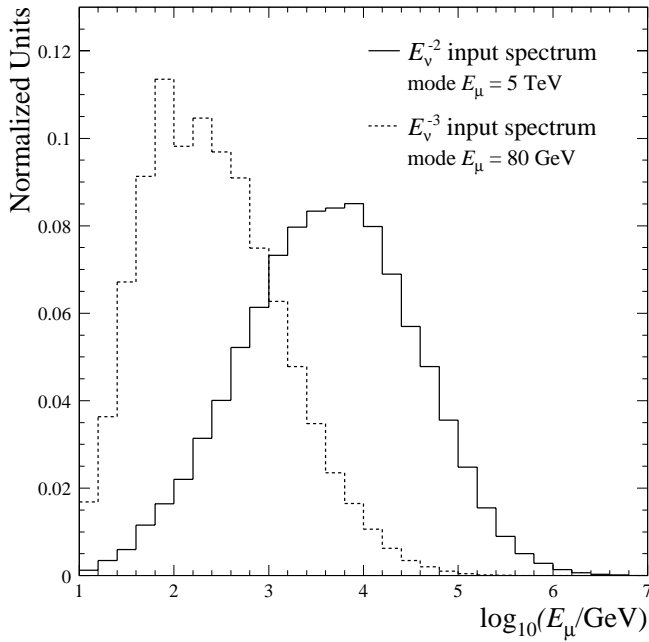


FIG. 14.—Neutrino-induced muon energy distribution at the detector. The differential neutrino spectra used as input for the simulation are proportional to E^{-2} (solid curve) and E^{-3} (dashed curve), respectively. The most probable energy for each distribution is shown.

The quantity $\mu_s(N_0, N_{\text{bgr}})$ is the upper limit on the number of signal events at the 90% confidence level, calculated following the unified procedure of Feldman & Cousins (1998), where N_0 is the observed number of events in a potential source bin and N_{bgr} is the expected number of background events. For the binning technique employed in our point-source search, N_{bgr} is determined by averaging the number of observed events over the declination band, excluding the bin being considered. The efficiency factor ϵ_{bin} accounts for the finite angular resolution and the possible noncentral location within the bin of a potential source. The factor T_{live} is the operational live time of the detector. The resulting muon and neutrino flux limits are shown in Figures 15 and 16, respectively, for various assumed spectral indexes between 2 and 3.

Figure 17 shows a comparison of the AMANDA flux limits with a representative sample of neutrino detectors located in the Northern Hemisphere. The AMANDA-B10 detector approaches its maximum sensitivity for declinations greater than $+30^\circ$, which complements the sky regions covered by neutrino detectors such as MACRO (Montaruli et al. 1999; Ambrosio et al. 2001; Perrone et al. 2001) and Super-Kamiokande (Matsuno et al. 2001).³³ With only 130.1 days of detector live time, the muon flux limits for positive declinations approach those achieved for the southern sky. The AMANDA flux limits were calculated for $E_\nu > 10$ GeV, while both Super-Kamiokande and MACRO present fluxes for $E_\mu > 1-2$ GeV, but for relatively hard differential neutrino spectra, such as E_ν^{-2} , the impact of energy threshold on muon flux limits is modest (Biron 2002).³⁴

In addition to the general search for a point source, a number of potential sources of particular interest were

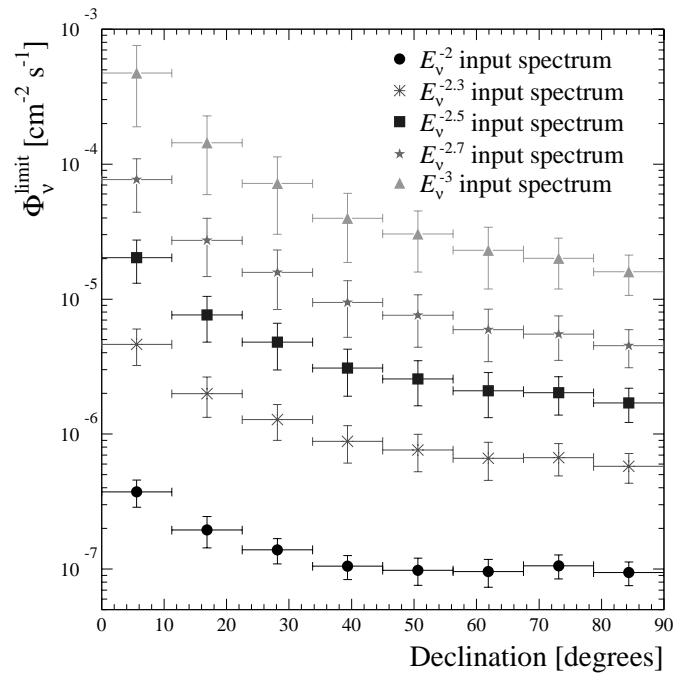


FIG. 15.—Neutrino flux limit (90% CL) for various spectral indexes. The results are shown as a function of declination, averaged over right ascension. Power-law exponent refers to the differential neutrino energy spectrum. The vertical error bars indicate the uncertainty obtained from systematic studies [See the electronic edition of the Journal for a color version of this figure.]

investigated by performing the significance test while centering the search bin on their sky coordinates. The resulting flux limits are presented in Table 2. As one interesting example, we compare the AMANDA limit on

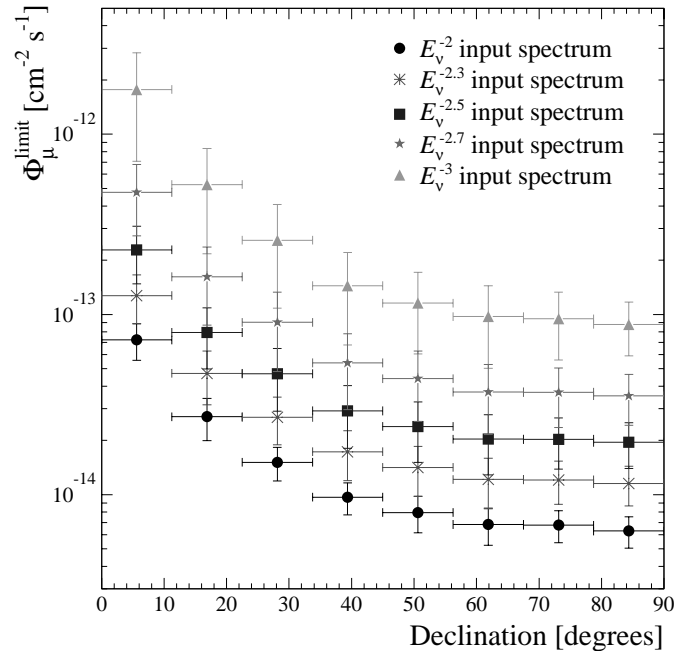


FIG. 16.—Neutrino-induced muon flux limit (90% CL) for various spectral indexes. The results are shown as a function of declination, averaged over right ascension. Note that the power-law exponent refers to the differential neutrino energy spectrum. [See the electronic edition of the Journal for a color version of this figure.]

³³ Available at http://www.copernicus.org/icrc/papers/ici7384_p.pdf.

³⁴ Available at <http://area51.berkeley.edu/manuscripts>.

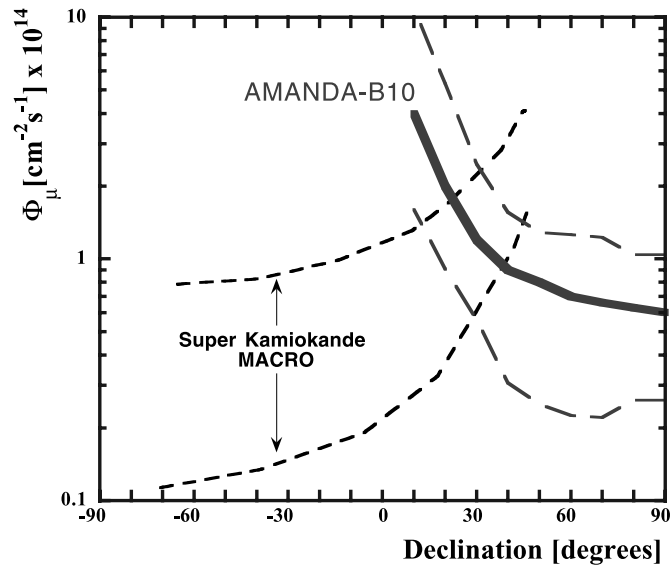


FIG. 17.—Upper limit on the muon flux (90% CL) as a function of declination. The solid curve is the AMANDA-B10 limit, averaged over right ascension, and the region delineated by the long-dashed curves provides a guide to the statistical fluctuation within the declination interval (see Table 4). The band defined by the short-dashed curves indicates the range of limits presented by MACRO (Montaruli et al. 1999; Ambrosio et al. 2001; Perrone et al. 2001) and Super-Kamiokande (Matsuno et al. 2001). [See the electronic edition of the *Journal* for a color version of this figure.]

the neutrino flux from Mrk 501 to the observed gamma-ray flux and this flux corrected for intergalactic absorption by infrared photons in Figure 18. Assuming that the neutrino energy spectrum is proportional to the inferred gamma-ray spectrum at the source, the AMANDA limit constrains the proportionality factor. For example, the ratio of the flux of neutrinos to the flux of gamma rays must be less than 10 if the source spectrum of Konopelko et al. (1999) is assumed. Recent work (de Jager & Stecker 2002) suggests that the ratio may be smaller.

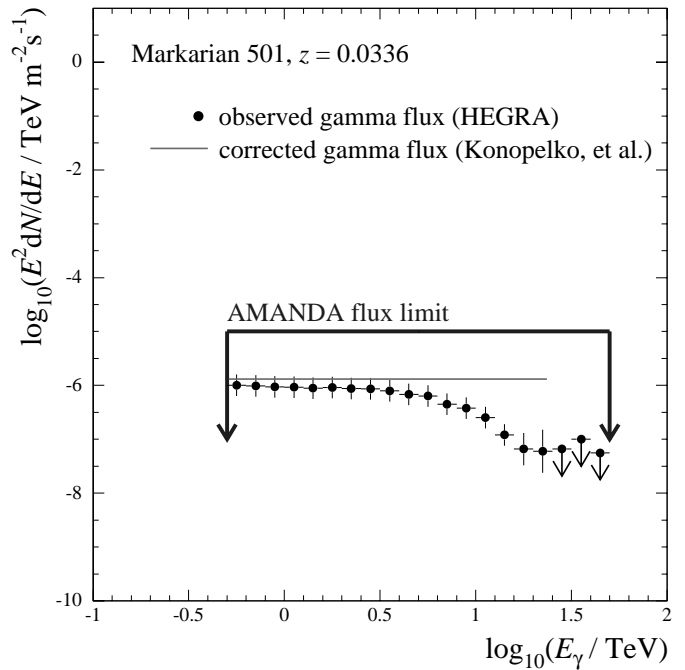


FIG. 18.—Time-averaged spectrum of gamma rays from Mrk 501 observed in 1997 (Aharonian et al. 1999; Krennrich et al. 1999) and corrected for intergalactic absorption by the diffuse infrared background (Konopelko et al. 1999). Gamma-ray flux is compared to the AMANDA neutrino limit assuming an energy dependence on the neutrino flux proportional to E^{-2} . [See the electronic edition of the *Journal* for a color version of this figure.]

8. IMPACT OF SYSTEMATIC UNCERTAINTIES ON FLUX LIMITS

In the absence of a well-understood source of high-energy neutrinos, the sensitivity of the AMANDA-B10 detector, as expressed in terms of the effective area and angular resolution, had to be estimated from detector simulations. The required input relies on knowledge of detector performance extracted from, e.g., laboratory measurements of the individual components, in situ measurements of the optical

TABLE 2
MUON AND NEUTRINO FLUX LIMITS ON SELECTED POINT SOURCES

Source	Model	N_0	N_{bgr}	ΔE (TeV)	$\Phi_{\nu}^{\text{limit}}$ ($10^{-8} \text{ cm}^{-2} \text{ s}^{-1}$)	$\Phi_{\mu}^{\text{limit}}$ ($10^{-15} \text{ cm}^{-2} \text{ s}^{-1}$)
Mrk 501	1	7	3.5	0.3–20	86.0	38.9
Mrk 501	2	7	3.5	1–1000	9.5	14.6
Mrk 421	3	4	3.7	1–1000	11.2	9.7
NGC 4151	3	5	3.6	1–1000	12.9	10.9
NGC 4151	4	5	3.6	60–2500	0.0042	5.6
1ES 2344	5	5	2.9	1–400	12.5	10.3
3C 66A	5	3	3.5	0.8–250	7.2	6.6
1ES 1959+650	5	4	1.7	0.8–250	13.2	9.7
Crab Nebula	5	2	5.6	1–1000	4.2	5.0
Cas A	5	3	2.2	1.8–1000	9.8	7.6
Cyg X-3	5	2	3.4	1–1000	4.9	4.6
Geminga	5	4	7.1	1.8–1000	6.8	9.1

NOTES.—Muon and neutrino flux limits on selected sources for $E_{\nu} > 10 \text{ GeV}$. The term N_0 is the number of observed events in the search bin, and N_{bgr} is the expected background. The energy interval ΔE contains 90% of the neutrino events, and the flux limits are corrected for systematic uncertainty (see § 8). Representative survey of models (second column): (1) neutrino spectrum identical to measured photon spectrum (Aharonian et al. 1999); (2) $d\Phi_{\nu}/dE \propto E_{\nu}^{-1.92}$; (3) Szabo & Protheroe 1992; (4) Stecker et al. 1991; (5) $d\Phi_{\nu}/dE \propto E_{\nu}^{-2}$.

TABLE 3
SYSTEMATIC UNCERTAINTY IN AMANDA-B10 EFFECTIVE AREA

Source of Systematic Uncertainty	Error in $\bar{A}_{\text{eff}}^{\mu}$ (%)
Angular dependence of OM sensitivity.....	± 25
Absolute OM sensitivity.....	± 15
Muon propagation.....	± 10
Calibration (timing and geometry).....	± 10
Hardware simplifications in detector simulation.....	$\pm < 10$
Optical properties of bulk ice.....	± 15

properties of the ice, and calibration studies. Consequently, the predicted sensitivity is affected by uncertainty in this information. Table 3 lists the dominant contributions to systematic uncertainties. The uncertainty in the right column is defined as the variation $|(A_{\text{eff}}^j - A_{\text{eff}}^{\text{nom}})/(A_{\text{eff}}^j + A_{\text{eff}}^{\text{nom}})|$ of the effective area from its value determined with the nominal set of input parameters, $A_{\text{eff}}^{\text{nom}}$, given by the area, A_{eff}^j , obtained by varying the specified parameter (index j) by its estimated uncertainty.

The most significant component is generated from the uncertainty in the angular dependence of the OM sensitivity. It arises mainly from a lack of detailed understanding of the physics governing the refreezing process in the water column required to be melted for the deployment of OMs. A local increase in scattering from air bubbles trapped in the vicinity of the OM translates into a modulation of its angle-dependent acceptance. This effect is difficult to disentangle from the intrinsic angular dependence of the OM sensitivity, which was measured in the laboratory. An event sample highly enriched in atmospheric muons was used to investigate the in situ angle dependence of the OM sensitivity (Ahrens et al. 2002a). The modification to the angular sensitivity leads to a 25% uncertainty in the effective area.

Since the angle-integrated sensitivity of the OM is a poorly constrained parameter in this analysis, we also investigated the impact of varying the absolute sensitivity of the OM. It was parameterized by a wavelength-dependent function that included the PMT quantum efficiency, the OM collection efficiency, obscuration by nearby cables, and absorption properties of the glass pressure vessel and coupling gel. We obtain a fractional uncertainty of 0.15 in the effective area after reducing the absolute OM sensitivity by 15%, a value consistent with the atmospheric neutrino results. Further reduction is inconsistent with observed experimental trigger rates.

As mentioned in § 4, two muon propagation routines were employed to show that systematic variations in the effective area for signal (i.e., upward-traveling) muons were between 5% and 10%. This is much less than observed for studies of atmospheric muons, presumably because of the much weaker angular dependence of the average path length. Possible uncertainties in timing and position calibration of individual OMs are included by varying these parameters to the largest extent allowed by the imprecision of the calibration procedures. The effective area changes by 10%. A conservative estimate of the variation in sensitivity introduced by uncertainties in the depth-dependent optical properties and their approximate treatment in the detector simulation is obtained by substituting the nominal bulk ice model, containing a parameterization of the measured dust strata, with a

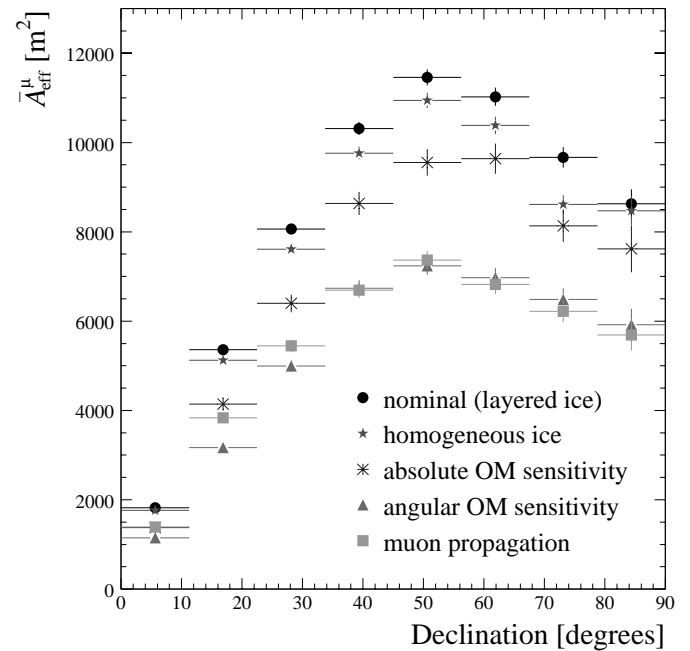


FIG. 19.—Comparison of average muon effective area for differential neutrino signal proportional to E^{-2} . See text for explanation of legend. Statistical uncertainty is indicated by vertical lines, unless it is obscured by the symbol. [See the electronic edition of the Journal for a color version of this figure.]

homogeneous ice model. The impact on effective area is less than 15%.

The impact of the most dominant systematic uncertainties on the average effective area is shown in Figure 19, where the systematic variations have been applied one at a time, with the exception of the muon propagation curve, which also includes the variation of the angular OM sensitivity.

The variation of the detector sensitivity due to systematic uncertainties was studied by adjusting the physical parameters in the detector simulation. The parameters were adjusted according to the known or estimated uncertainties listed in Table 3, which are assumed to bound the true values of the parameters. Systematic uncertainty was included according to the prescription of Conrad et al. (2003), which is an extension of the method of Cousins & Highland (1992). The calculations assumed that the distribution of systematic uncertainty was flat and bounded by the maximum and minimum values for a given declination bin, found in Figures 20 and 21.

The solid curves in Figures 20 and 21 indicate the flux limits after adjusting for systematic uncertainty. They are valid for declination greater than $+5^\circ$. The limits including systematic uncertainties are about 25% worse than those obtained from the simulation with nominal input parameters. Finally, the flux limits change by less than 6% because of the effects of zenith offset and the variation in Ψ_{median} due to declination (Young 2001). These small effects were not taken into consideration in the limit calculations.

9. DISCUSSION

The previous sections have shown that AMANDA-B10 has unprecedented sensitivity to high-energy neutrinos and possesses the necessary angular response and background

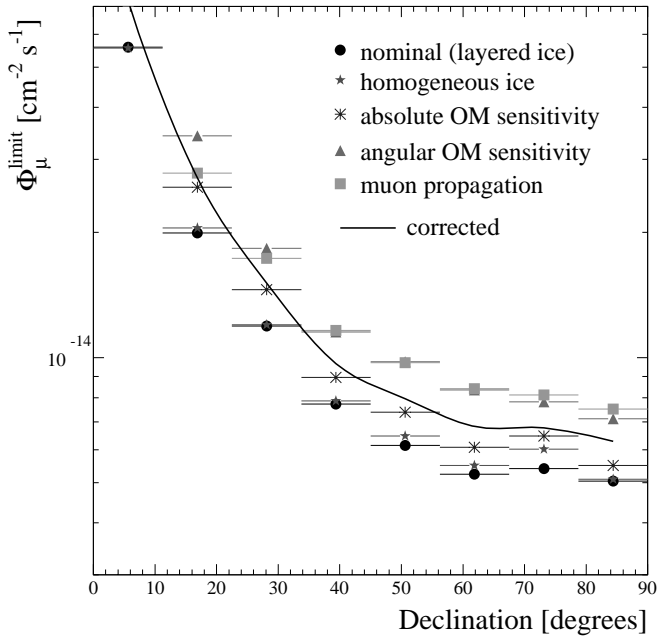


FIG. 20.—Comparison of muon flux calculations for differential neutrino signal proportional to E^{-2} . See text for explanation of legend. Statistical uncertainty is small and not shown. The solid curve (corrected) includes systematic uncertainty and indicates the final result of this work. [See the electronic edition of the Journal for a color version of this figure.]

rejection to search for point emission of these particles from astronomical objects; i.e., it is a novel telescope that detects the neutrino messenger. The sensitivity and angular response were determined by simulation. The reliability of these programs was established by utilizing the known signals generated by (downgoing) atmospheric muons and (upgoing) atmospheric neutrinos. The angular response was

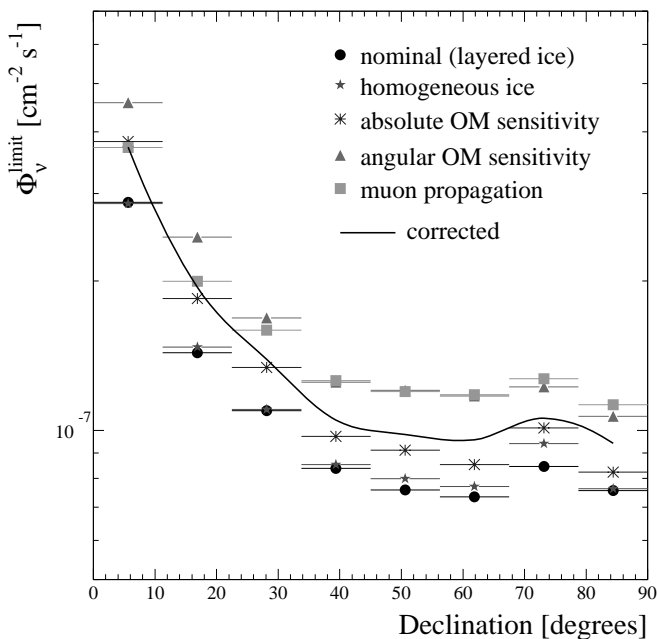


FIG. 21.—Comparison of neutrino flux calculations for differential neutrino signal proportional to E^{-2} . See text for explanation of legend. Statistical uncertainty is small and not shown. The solid curve (corrected) includes systematic uncertainty and indicates the final result of this work. [See the electronic edition of the Journal for a color version of this figure.]

confirmed by the study of air shower events that triggered both AMANDA-B10 and SPASE. Systematic uncertainty in the analysis procedure was also addressed.

The search for point sources of high-energy neutrinos revealed no candidates. A set of event selection criteria was determined by optimizing the signal-to-noise ratio for a signal with a hard energy spectrum, yet this analysis retains reasonable sensitivity for softer spectra. The upper limits on muon flux for all search bins in the northern hemisphere are presented in Table 4.

The neutrino flux limits in Figure 15 are inferred from the assumption of a power-law energy spectrum. This procedure is reliable if the mean energy of the neutrino-induced muon is compatible with the energy response of the detector. For example, Figure 14 shows that E_μ at the detector brackets the interval between 0.1 and 10^3 TeV for source spectra proportional to E^{-2} . Two lines of evidence show that the simulated energy response of the detector is valid over this interval. First, the agreement between the detected and expected rates of atmospheric neutrinos shows that the response of AMANDA is being correctly modeled in the sub-TeV region. Second, the tails of the N_{ch} -distribution are sensitive to brighter events within AMANDA, which are roughly equivalent to single muons with energy above 1 TeV. We know of no reason to doubt the predicted energy response for $E_\mu < 10^3$ TeV. Evaluation and calibration of the energy response beyond 10^3 TeV remain an ongoing activity.

Not all model predictions are well characterized by power-law energy spectra. Therefore, Table 2 shows the results for a selection of models in the literature. The inferred limits on neutrino flux apply to point sources with continuous emission (or episodic emission averaged over the time interval of data collection) and power-law energy spectra with a fixed spectral index. The limits presented here for sources at large positive declination complement existing data, so that comparable limits now exist for the entire sky.

During 1997, the TeV gamma-ray emission of two nearby AGN blazars (Mrk 421 and 501) were observed to exhibit episodic flaring. If neutrino emission follows the same time variability, then it may be possible to improve the signal-to-noise ratio by eliminating the periods of relatively low output. Multiple detections of Mrk 501 from several air Cerenkov instruments allowed nearly continuous monitoring, including periods when the Moon was shining. However, monitoring by multiple instruments extended only from March to late August. Because of uncertainties in the details of the time dependence of the gamma-ray emission, neutrino flux limits are not greatly improved by restricting the analysis to high-flux periods of gamma-ray emission.

While this paper describes an analysis dedicated to the search for point sources, another strategy was developed based on the event selection of the atmospheric neutrino analysis (Biron 2002). The results of this complementary analysis are consistent with the results presented here. The absolute efficiency was extracted by comparing to the known flux from atmospheric neutrinos. Moreover, the second analysis was subject to different systematic uncertainties.

The method based on the atmospheric neutrino analysis retained a smaller event sample of 369 events, of which ~ 270 are expected from atmospheric neutrinos. The cut selections produce an implicit optimization on more vertical

TABLE 4
MUON FLUX LIMITS

Decl. (deg)	R.A. (hours)	$\Phi_{\mu}^{\text{limit}}$ ($10^{-15} \text{ cm}^{-2} \text{ s}^{-1}$)	Decl. (deg)	R.A. (hours)	$\Phi_{\mu}^{\text{limit}}$ ($10^{-15} \text{ cm}^{-2} \text{ s}^{-1}$)	Decl. (deg)	R.A. (hours)	$\Phi_{\mu}^{\text{limit}}$ ($10^{-15} \text{ cm}^{-2} \text{ s}^{-1}$)
85.....	4.0	2.5	39.....	7.8	6.1	17.....	7.9	9.0
	12.0	6.5		8.9	2.5		8.7	9.0
	20.0	10.5		9.9	15.5		9.5	19.9
73.....	1.3	6.9		11.0	13.5		10.3	14.9
	4.0	4.2		12.0	13.5		11.2	42.6
	6.7	2.1		13.0	8.0		12.0	11.9
	9.3	6.9		14.1	8.0		12.8	34.1
	12.0	13.7		15.1	8.0		13.7	24.6
	14.7	6.9		16.2	10.6		14.5	42.6
	17.3	9.6		17.2	15.5		15.3	8.9
	20.0	4.2		18.3	3.9		16.1	11.9
	22.7	4.2		19.3	6.1		17.0	14.9
62.....	0.9	7.9		20.3	10.6		17.8	8.9
	2.6	5.5		21.4	3.9		18.6	42.6
	4.3	12.1		22.4	3.9		19.4	19.9
	6.0	3.4		23.5	6.1		20.3	19.9
	7.7	7.9	28.....	0.4	20.5		21.1	48.0
	9.4	5.5		1.3	20.5		21.9	14.9
	11.1	7.9		2.2	7.1		22.8	34.1
	12.9	1.9		3.1	13.9		23.6	29.1
	14.6	5.5		4.0	24.0	6.....	0.4	33.6
	16.3	3.5		4.9	13.9		1.2	64.9
	18.0	3.5		5.8	7.1		2.0	127.2
	19.7	7.9		6.7	20.5		2.8	64.9
	21.4	7.9		7.6	13.9		3.6	47.8
	23.1	9.9		8.4	20.5		4.4	33.6
51.....	0.6	7.7		9.3	7.1		5.2	96.1
	1.9	10.0		10.2	24.0		6.0	64.9
	3.2	2.2		11.1	20.5		6.8	78.0
	4.4	7.7		12.0	24.0		7.6	78.0
	5.7	5.9		12.9	5.4		8.4	47.8
	6.9	10.0		13.8	13.9		9.2	64.9
	8.2	2.2		14.7	5.4		10.0	64.9
	9.5	10.0		15.6	20.5		10.8	127.2
	10.7	5.9		16.4	16.7		11.6	47.9
	12.0	1.6		17.3	5.4		12.4	33.6
	13.3	10.0		18.2	16.7		13.2	143.5
	14.5	5.9		19.1	7.1		14.0	24.9
	15.8	10.0		20.0	10.2		14.8	47.8
	17.1	7.7		20.9	7.1		15.6	33.6
	18.3	14.1		21.8	13.9		16.4	64.9
	19.6	3.9		22.7	10.2		17.2	47.8
	20.8	5.9		23.6	7.1		18.0	47.8
	22.1	12.4	17.....	0.4	48.0		18.8	112.4
	23.4	7.7		1.2	34.1		19.6	96.1
39.....	0.5	10.6		2.1	14.9		20.4	33.6
	1.6	15.5		2.9	51.9		21.2	96.1
	2.6	8.0		3.7	19.9		22.0	24.9
	3.7	13.5		4.6	24.6		22.8	64.9
	4.7	3.9		5.4	14.9		23.6	78.0
	5.7	15.5		6.2	4.5			
	6.8	6.1		7.0	9.0			

NOTES.—Neutrino-induced muon flux upper limits for source spectra proportional to E^{-2} . The impact of systematic uncertainty is included. Angular coordinates refer to the center of the search bin.

events and/or softer energy spectra. Figure 22 compares the average effective area of the two analyses for an assumed differential spectra proportional to E^{-2} . The best flux limits for soft spectra are obtained by atmospheric neutrino analysis, but the neutrino and muon flux limits for either analysis are much larger than obtained for an assumed power law of an index of -2.0 .

While the flux limits for any particular source or direction in the northern hemisphere can be extracted from this analysis (see Table 4), flux limits, both integral and pseudodifferential, for a preselected list of 62 sources have been reported (Biron 2002). These include all known TeV gamma-ray blazars, nearby QSOs, and Galactic TeV gamma-ray sources in the northern hemisphere. The list also includes

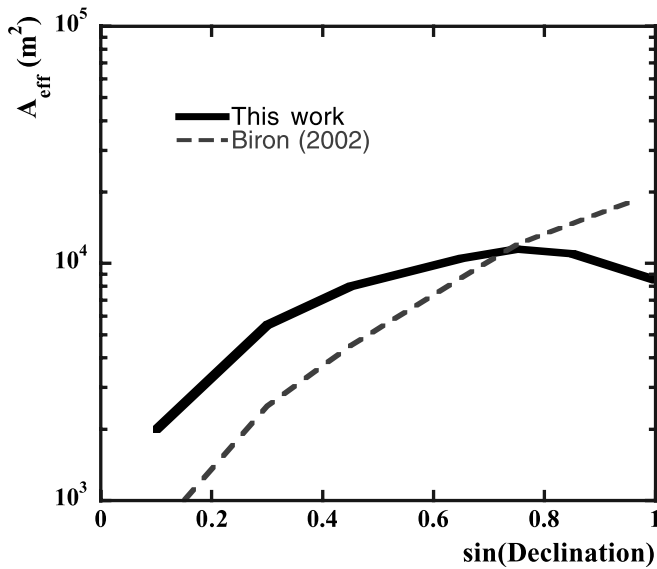


FIG. 22.—Comparison of average muon effective area as a function of declinations for differential neutrino signal proportional to E^{-2} . The dashed curve is from Biron (2002). Neither curve includes the effect of systematic uncertainties. [See the electronic edition of the *Journal* for a color version of this figure.]

microquasars, the five most luminous AGNs in wavelength bands that span across MeV, X-ray, infrared, and radio bands. Of particular interest are radio galaxies with strong emission at GHz frequencies. We have also investigated BL Lac objects that are close to the arrival directions of the very highest energy cosmic rays (Tinyakov & Tkachev 2001) and the 10 reported cosmic-ray doublets at extreme energies (Uchihori et al. 2000).

10. FUTURE

The technique employed in this paper optimized the selection criteria on signal to noise. Because of the relatively large number of sky bins and the relatively low number of events in any individual bin, the analysis procedure produced event samples that are dominated by poorly recon-

structed atmospheric muons rather than upward-traveling atmospheric neutrino background. However, as the background rejection of downgoing events improves with larger detectors, such as AMANDA-II, this trend may not continue.

AMANDA-II, completed in 2000 January, surrounds the B10 core with nine additional strings, more than doubling the number of optical modules. For this broader configuration, the effective area for neutrino-induced muons remains relatively constant over the entire hemisphere (Barwick et al. 2001).³⁵ Consequently, AMANDA-II is expected to achieve a factor of 5 improvement in sensitivity for nearly horizontal events compared to AMANDA-B10 (Wischnewski et al. 2001).³⁶ The greater statistical sample of atmospheric neutrinos will allow better tests of the detector simulation programs, especially near the horizon. With the data already collected on tape, AMANDA-II can observe (or exclude) neutrino fluxes that are approximately 1 order of magnitude below the limits presented here, as shown in Figure 1.

This research was supported by the following agencies: the US National Science Foundation Office of Polar Programs and Physics Division; the University of Wisconsin Alumni Research Foundation; the US Department of Energy; the Swedish Natural Science Research Council; the Swedish Polar Research Secretariat; the Knut and Alice Wallenberg Foundation, Sweden; the German Ministry for Education and Research; the US National Energy Research Scientific Computing Center (supported by the Office of Energy Research of the US Department of Energy); the University of California, Irvine, AENEAS Supercomputer Facility; and the Deutsche Forschungsgemeinschaft (DFG). C. Pérez de los Heros received support from the EU fourth framework of Training and Mobility of Researchers, and D. F. Cowen acknowledges the support of the NSF CAREER program. P. Desiati was supported by the Koerber Foundation.

³⁵ Available at http://area51.berkeley.edu/manuscripts/20010601xx-ICRC_AmIIv3.pdf.

³⁶ Available at http://area51.berkeley.edu/manuscripts/20010602xx-icrc2001_aai.pdf.

REFERENCES

- Agrawal, V., Gaisser, T., Lipari, P., & Stanev, T. 1996, *Phys. Rev. D*, 53, 1314
- Aharonian, F. A., et al. 1999, *A&A*, 349, 11
- Ahrens, J., et al. (AMANDA Collaboration). 2002a, *Phys. Rev. D*, 66, 012005
- . 2002b, *Phys. Rev. D*, 66, 032006
- . 2002c, *Phys. Rev. D*, submitted (astro-ph/0206487)
- Ambrosio, M., et al. (MACRO Collaboration). 2001, *ApJ*, 546, 1038
- Andres, E., et al. 2000, *Astropart. Phys.*, 13, 1
- . 2001, *Nature*, 410, 441
- Barbagli, G., et al. 1993, *Nucl. Phys. B (Proc. Suppl.)*, 32, 156
- Barwick, S. W., et al. (AMANDA Collaboration). 2000, *Nucl. Phys. B (Proc. Suppl.)*, 87, 402
- . 2001, *Proc. 27th Int. Cosmic-Ray Conf. (Hamburg)*, 2, 1101
- Bednarek, W., & Protheroe, R. J. 1999, *MNRAS*, 302, 373
- Berezinsky, V. S., & Dokuchaev, V. I. 2001, *Astropart. Phys.*, 15, 87
- Biron, A. 2002, Ph.D. thesis, Humboldt Univ. Berlin
- Bouchta, A., et al. (AMANDA Collaboration). 1999, *Proc. 26th Int. Cosmic-Ray Conf. (Salt Lake City)*, 2, 108
- Boziev, S. N., et al. 1989, preprint (INR preprint P-0630)
- Buckley, J. H., et al. 1998a, *Adv. Space Res.*, 21, 101
- Buckley, J. H., et al. 1998b, *Science*, 279, 676
- Catanese, M., & Weekes, T. C. 1999, *PASP*, 111, 1193
- Conrad, J., Botner, O., Hallgren, A., & Pérez de los Heros, C. 2003, *Phys. Rev. D*, in press (hep-ex/0202013)
- Cousins, R. D., & Highland, V. L. 1992, *Nucl. Instrum. Methods Phys. Res. A*, 320, 331
- de Jager, O. C., & Stecker, F. W. 2002, *ApJ*, 566, 738
- Dermer, C. D. 1999, *Astropart. Phys.*, 11, 1
- Dermer, C. D., & Atayan, A. 2001, *Phys. Rev. Lett.*, 87, 221102
- Dickinson, J. E., et al. 2000, *Nucl. Instrum. Methods Phys. Res. A*, 440, 95
- Distefano, C., Guetta, D., Waxman, E., & Levinson, A. 2002, *ApJ*, 575, 378
- Feldman, G. J., & Cousins, R. D. 1998, *Phys. Rev. D*, 57, 3873
- Gaisser, T. K. 2002, *Astropart. Phys.*, 16, 285
- Hardtke, R., & Barouch, G. (for the AMANDA Collaboration). 2001, *Proc. 27th Int. Cosmic-Ray Conf. (Hamburg)*, 2, 1121
- Heck, D., et al. 1998, Rep. FZKA 6019 (Forschungszentrum Karlsruhe)
- . 1999, in *Simulations and Analysis Methods for Large Neutrino Telescopes*, ed. C. Spiering (DESY-PROC-1999-01; Zeuthen: DESY), 228
- Hill, G. 1997, *Astropart. Phys.*, 6, 215
- Hill, G., & Leuthold, M. (for the AMANDA Collaboration). 2001, *Proc. 27th Int. Cosmic-Ray Conf. (Hamburg)*, 2, 1113
- Hundertmark, S., et al. (AMANDA Collaboration). 1999, *Proc. 26th Int. Cosmic-Ray Conf. (Salt Lake City)*, 2, 12
- Karle, A., et al. 2003, *Proc. XXth Int. Conf. Neutrino Physics and Astrophysics (Amsterdam: North-Holland)*, in press (astro-ph/0209556)
- Konopelko, A. K., Kirk, J. G., Stecker, F. W., & Mastichiadis, A. 1999, *ApJ*, 518, L13

- Krennrich, F., et al. 1999, *ApJ*, 511, 149
- Learned, J. G., & Mannheim, K. 2000, *Annu. Rev. Nucl. Part. Sci.*, 50, 679
- Levinson, A., & Waxman, E. 2001, *Phys. Rev. Lett.*, 87, 171101
- Lipari, P., & Stanev, T. 1991, *Phys. Rev. D*, 44, 3543
- Lohmann, W., Kopp, R., & Voss, R. 1985, preprint (CERN preprint CERN-85-03)
- Matsuno, S., et al. (Super-Kamiokande Collaboration). 2001, *Proc. 27th Int. Cosmic-Ray Conf. (Hamburg)*, 2, 1065
- Montaruli, T., et al. (MACRO Collaboration). 1999, *Proc. 26th Int. Cosmic-Ray Conf. (Salt Lake City)*, 2, 213
- Nellen, L., Mannheim, K., & Biermann, P. L. 1993, *Phys. Rev. D*, 47, 5270
- Oppelt, A. 2001, Ph.D. thesis, Univ. Méditerranée Aix-Marseille II
- Perrone, L., et al. (MACRO Collaboration). 2001, *Proc. 27th Int. Cosmic-Ray Conf. (Hamburg)*, 2, 1073
- Rachen, J. P. 2000, preprint (astro-ph/0003282)
- Rawlins, K. 2001, Ph.D. thesis, Univ. Wisconsin, Madison
- Rhode, W., & Chirkin, D. 2001, *Proc. 27th Int. Cosmic-Ray Conf. (Hamburg)*, 3, 1017
- Spiering, C. 2001, *Proc. 27th Int. Cosmic-Ray Conf. (Hamburg)*, 2, 1242
- Stecker, F. W., Done, C., Salamon, M. H., & Sommers, P. 1991, *Phys. Rev. Lett.*, 66, 2697 (erratum 69, 2738 [1992])
- Stecker, F. W., & Salamon, M. H. 1996, *Space Sci. Rev.*, 75, 341
- Szabo, A. P., & Protheroe, R. J. 1992, in *Proc. Workshop on High Energy Neutrino Astrophysics*, ed. V. J. Stenger, J. G. Learned, S. Pakvasa, & X. Tata (Singapore: World Scientific), 24
- Tinyakov, P. G., & Tkachev, I. I. 2001, *J. Exp. Theor. Phys. Lett.*, 74, 445
- Uchiyori, Y., et al. 2000, *Astropart. Phys.*, 13, 151
- Weekes, T. 2001, *AIP Conf. Proc.* 558, *High Energy Gamma-Ray Astronomy*, ed. F. A. Aharonian & H. Völk (Melville: AIP), 15
- Wiebel-Sooth, B., & Biermann, P. L. 1998, in *Landolt-Börnstein New Series, Group VI, Vol. 3C* (Berlin: Springer), 37
- Wischniewski, R., et al. (AMANDA Collaboration). 1999a, *Nucl. Phys. B (Proc. Suppl.)*, 75 (1–2), 412
- . 2001, *Proc. 27th Int. Cosmic-Ray Conf. (Hamburg)*, 2, 1105
- Woschnagg, K., et al. (AMANDA Collaboration). 1999, *Proc. 26th Int. Cosmic-Ray Conf. (Salt Lake City)*, 2, 200
- Young, S. 2001, Ph.D. thesis, Univ. California, Irvine